Master's Thesis
석사 학위논문

Vortex pinning force in superconducting Na-intercalated $Ca_{10}Na_x(Pt_3As_8)(Fe_2As_2)_5$ single crystal

Soyeon Shin(신 소 연 辛 昭 娟)

Department of Emerging Materials Science

신물질과학전공

DGIST

2015

Vortex pinning force in superconducting Na-intercalated $Ca_{10}Na_x(Pt_3As_8)(Fe_2As_2)_5$ single crystal

Advisor : Professor Jung-Il Hong

Co-Advisor : Professor Keeseong Park

by

Soyeon Shin

Department of Emerging Materials Science

DGIST

A thesis submitted to the faculty of DGIST in partial fulfillment of the requirements for the degree of Master of Science in the Department of Emerging Materials Science. The study was conducted in accordance with Code of Research Ethics[1].

12. 02. 2014

Approved by

Professor Jung-Il Hong (S i g n a t u r e)

(Advisor)

Professor Keeseong Park (S i g n a t u r e)

(Co-Advisor)

[1] Declaration of Ethical Conduct in Research: I, as a graduate student of DGIST, hereby declare that I have not committed any acts that may damage the credibility of my research. These include, but are not limited to: falsification, thesis written by someone else, distortion of research findings or plagiarism. I affirm that my thesis contains honest conclusions based on my own careful research under the guidance of my thesis advisor.

Vortex pinning force in superconducting Na-intercalated $Ca_{10}Na_x(Pt_3As_8)(Fe_2As_2)_5$ single crystal

Soyeon Shin

Accepted in partial fulfillment of the requirements for the degree of Master of Science.

12. 02. 2014

Head of Committee_____(인)

Prof. Jung-Il Hong

Committee Member_____(인)

Prof. Keeseong Park

Committee Member_____(인)

Prof. Jungpil Seo

MS/EM

201321011

신 소 연. Soyeon Shin. Vortex pinning force in superconducting Na-intercalated $Ca_{10}Na_x(Pt_3As_8)(Fe_2As_2)_5$ single crystal. Department of Emerging Materials Science. 2015. 54p. Advisor Prof. Jung-Il Hong. Co-Advisor Prof. Keeseong Park.

ABSTRACT

Discovery of the iron arsenide family with high superconducting transition temperature (T_c) naturally raised the question about the relationships between them and cuprates. Since the LaFeAsOF superconductors was discovered, various types of iron-based superconductors(IBSs) with layered structures have been actively investigated. Recently, new type of IBSs, $Ca_{10}(Pt_3As_8)(Fe_2As_2)_5$ superconductors is discovered by Ni.*et al.* in 2012. This superconductor has a new layer of PtAs. The parent compound of $Ca_{10}(Pt_3As_8)(Fe_2As_2)_5$ superconductor do not show superconductivity. The $Ca_{10}(Pt_3As_8)(Fe_2As_2)_5$ was only reported so far the properties of electron doped superconductors.

In this thesis, we grew single crystals of $Ca_{10}Na_x(Pt_3As_8)(Fe_2As_2)_5$ superconductors, employing the Bridgman method. And we have analyzed on the relationships between critical current density (J_c) and magnetization hysteresis loops based on the Bean critical state model. It was clearly shown that $Ca_{10}Na_x(Pt_3As_8)(Fe_2As_2)_5$ single crystal has the point defect pinning center due to the inclusion of the Na-ions in the single crystalline $Ca_{10}Na_x(Pt_3As_8)(Fe_2As_2)_5$.

Key word: single crystal, superconductor, vortex, critical current density, flux pinning

Contents

List of Tables

List of Figures

Chapter 1. Introduction

The discovery of superconductivity by Heike Kamerlingh Onnes was approached by liquefying the helium. He found that the electrical resistance of the mercury fell to zero at 4.2 K in 1911 [1].

In 1933, Meissner and Oschsenfeld had discovered that when a superconducting sample is placed in a magnetic field and then cooled below the superconducting transition temperature(T_c), the magnetic flux is ejected completely from the sample. This means that the magnetic field strength falls to zero within a superconductor and this is called the Meissner effect [2]. Since the superconductivity phenomenon was announced, many scientists released important findings. As with as Start of the two fluid model[3] in 1934 by C. J. Gorter and H. G. B. Casimir, London theory[4] was published by the brothers Fritz and Heinz London by in 1935. In 1950, the Ginzburg-Landau theory [5] of superconductivity was developed by Landau and Ginzburg. The complete microscopic theory of superconductivity which is suggested by by Bardeen, Cooper and Schrieffer (BCS theory)[6] was finalized in 1957. This BCS theory explained the superconducting current as a superfluid of Cooper pairs, pairs of electrons interacting through the exchange of phonons. With this study, Bardeen, Cooper and Schrieffer were awarded the Nobel Prize in 1972. However, the biggest problem of the superconductors, was the extremely low transition temperatures that required the use of cryogenic system. Therefore the industrial applications of the superconductivity has been limited. Thus, during the past 110 years, scientists have focused on the development of high superconducting transition temperature superconductors. Early studies statred with the pure metals or

double element alloys but their T_c was limited to a relatively low critical temperatures.

However, 70 years later, Bendnorz and Muller observed compound LaBaCuO which exhibits T_c of over 30 K [7].

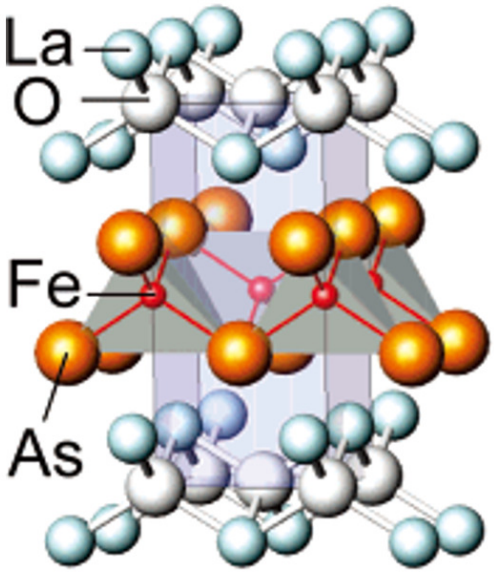

Figure 1.1: Crystal structure of LaOFeAs [10]

Then, high-temperature superconductors attracted significant attentions by many researchers around the world, and T_c of up to 135 K [8] at atmospheric pressure and 164 K under high pressure[9] was achieved within a few years. In the case of copper-oxide-based(cuprates) superconductor, it was difficult to use in industry because it shows very large anisotropy in crystalline structure, a short coherence length, and fragile mechanical properties. Therefore, it was crucial to find out high-T_c superconductors other than the cuprates superconductors.

The Iron-based superconductors (IBSs) first discovery by H. Hosono group in early 2008, near the T_c of 26 K was reported in F doping LaFeAsO [Fig1.1][10]. Since then, intensive efforts to develop iron-based high-T_c superconductors have been conducted steadily [Fig1.2][11]. Iron-based high-temperature superconductors can be largely di-

vided into five groups since it was found [Fig1.3][12]. In commonly, all groups of IBSs, there is the FeAs(Se) layer.

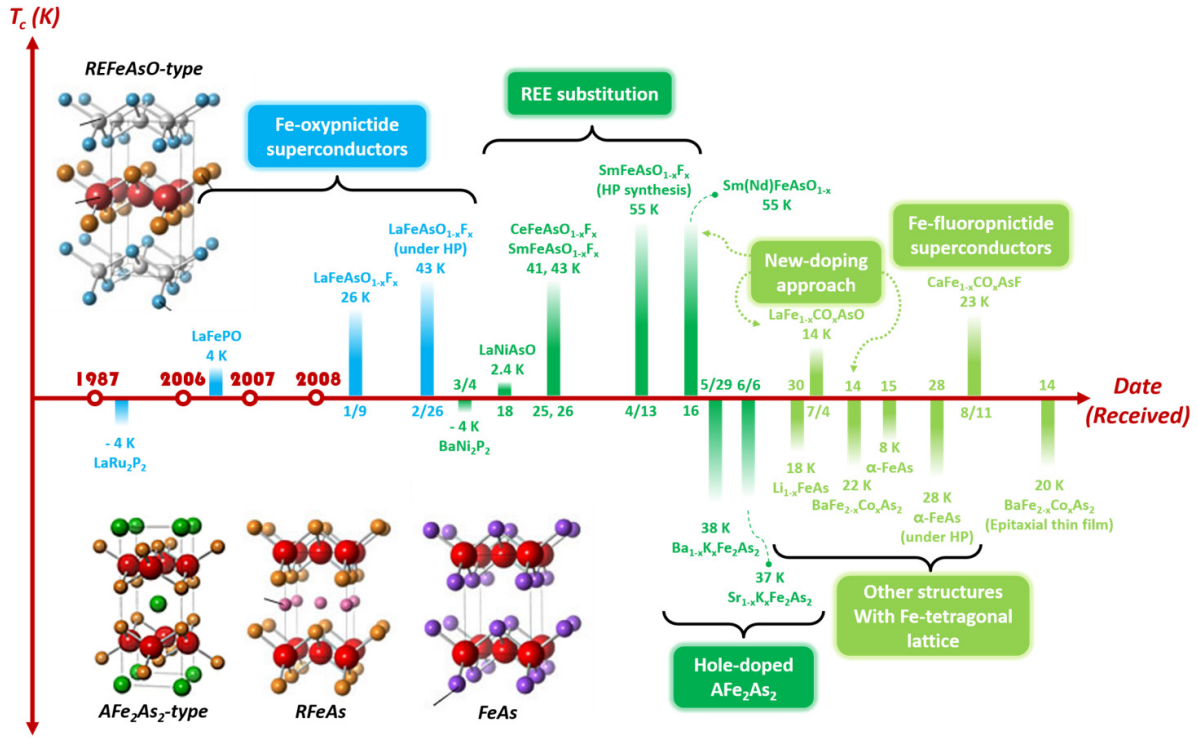

Figure 1.2: Progress in Iron-based superconductors (IBSs)[11].

Superconductivity had been classified on type of two according to the magnetization. Type-1 superconductors are existing only below T_c and below a critical magnetic field(H_c) strength. If the type-1 superconductors reach at H_c, Meissner effect vanishes as soon as within type-1 superconductors. This type also is described well by the BCS theory. The type-2 superconductors were starting in 1930 with lead-bismuth alloys. This type was different from type-1 superconductors that in case of type-2 superconductors were exhibited the mixed state or vortex state. Due to the mixed state or vortex state, type-2 superconductor has much higher critical field which makes it possible to carry much higher current densities. For this reason, the type-2 superconductors compared with the type-1 superconductors, the type-2 of H_{c2} is stronger than the type-1 of H_c the strength

of the critical magnetic field. Therefore type-2 superconductor could carry much higher current densities than type-1 in the superconducting state.

Due to these characteristics in the type-2 superconductors, when applying in industrial fields, is useful to be used from type-2 superconductors such as the fabrication of the superconducting coil, superconducting magnets, *etc.* In case of utilized superconductors in electrical industrial fields, it should have a high critical current density or high critical fields. The presence of vortex in the type-2 superconductors, it causes the critical current density of low value. If an electric current is applied through the superconductor then, the vortex is moving by the Lorentz force. At this time, the vortex motion by the thermal fluctuation is to reduce the critical current density by destroying the superconducting state. This being so, it is important to grabbing a vortex motion. One of the methods in order to prevent the vortex motion makes the pinning source on the inside superconductors. Thus, the study of vortex pinning mechanism is an essential research to industrial applications of superconductors.

In chapter 2, the basic theory of superconductivity, critical state model and flux pinning model are briefly described. Chapter 3 detailedly explains fabrication method of single crystals and also we described roughly for measurement methods and measuring equipment used in chapter 4. Based on this measurement, we will be discussed in chapter 5 as following the respects. We will obtain the superconducting transition temperature, and value of the critical current density and the flux pinning force will be analyzed how have changed compared with the existing published $Ca_{10}(Pt_3As_8)(Fe_2As_2)_5$, by adding the Na impurities in $Ca_{10}(Pt_3As_8)(Fe_2As_2)_5$ single crystals. Finally, the summary of this thesis will be remarked in the last chapter.

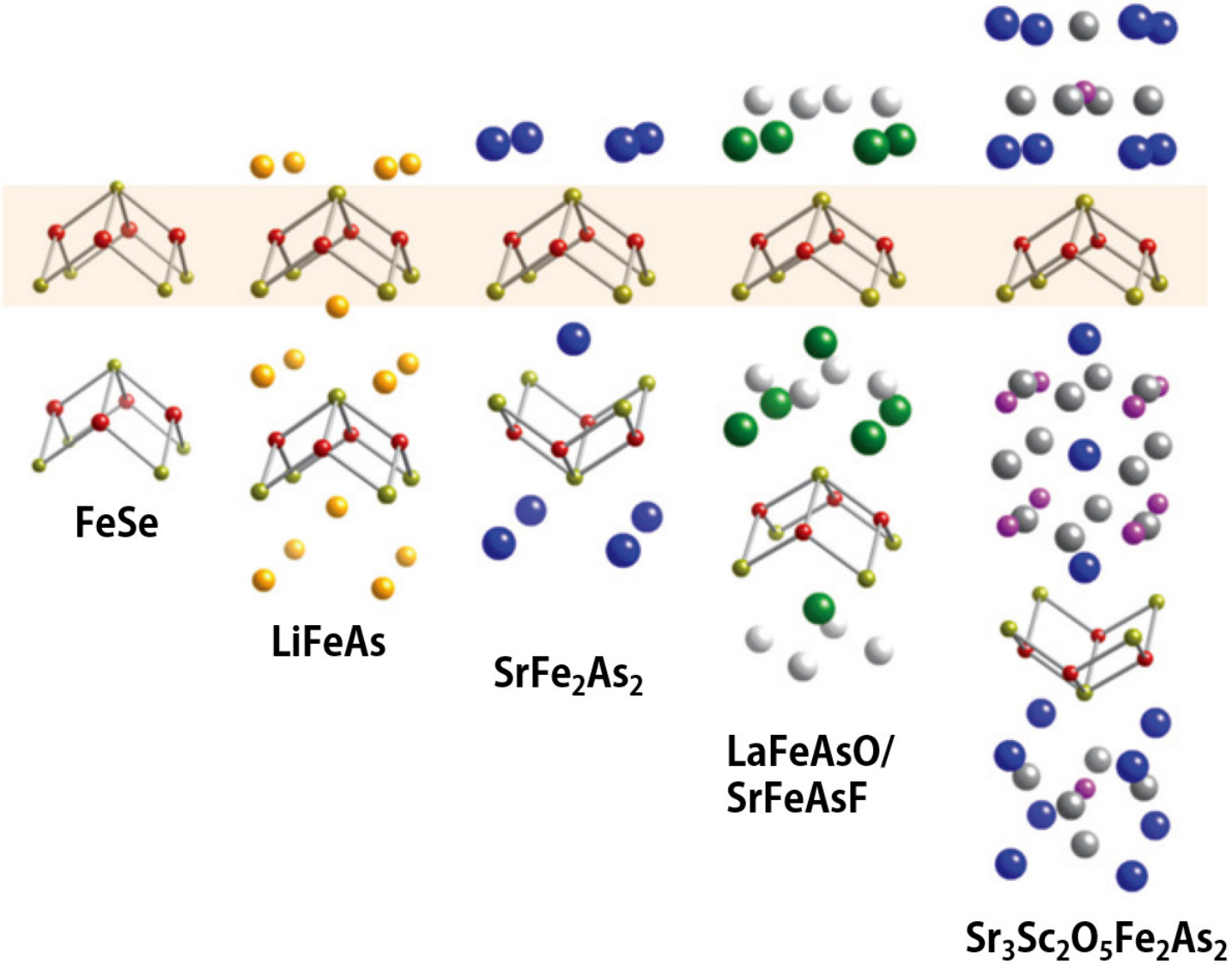

Figure 1.3: Crystallographic of the iron-based superconductors, the representative tetragonal structures[12].

Chapter 2. Theory

2.1 Superconductivity

In 1908, Heike Kamerlingh Onnes became the first person who succeeded in liquefying helium. After three years, superconductivity was observed first by him in 1911 from mercury (Hg) at 4.21 K [Fig2.1]. Eventually, he won a Nobel Prize in physics by discovery of superconductivity in 1913[13].

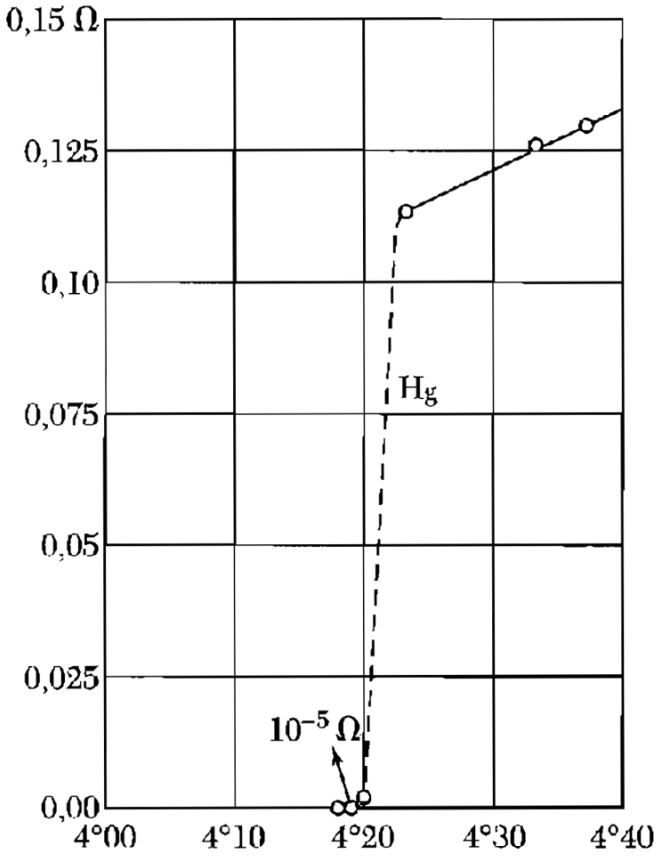

Figure 2.1: Resistance in ohms of a mercury versus absolute temperature[13].

Fundamentally, superconductivity is the phenomenon where the electrical resistivity drops abruptly to zero and the Meissner effect appears. These two properties are impor-

tant hallmarks of superconductivity. Superconductivity shows the 'perfect' conductivity which means that the that electrical resistivity is zero (R=0) below a certain temperature. This a special temperature is called the critical temperature or superconducting transition temperature (T_c).

According to the characteristic of the material, the electrical resistivity exhibits the complete disappearance [Fig2.2(a)]. Normally pure elemental material shows very sharp transition. On the other hand, materials including impurities exhibit rather broad transitions. The perfect conductivity of superconductor was proved from the measurement of persistent electrical current through the ring shaped superconductor.

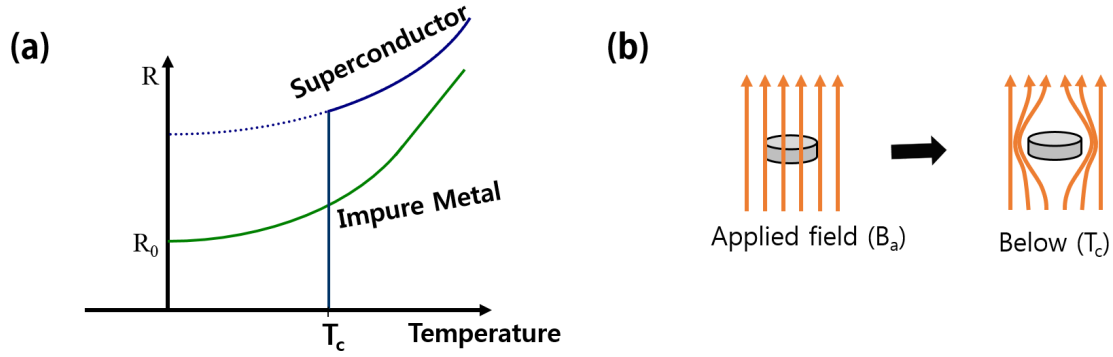

Figure 2.2: The properties of superconductivity. (a) Resistivity of superconductor and metal, and (b) Meissner effect in a superconductor, which is cooled in a constant applied magnetic field[14].

The Meissner effect is related to the magnetic properties and it distinguishes a superconductor from a perfect conductor. When a superconductor is cooled below the transition temperature under an applied magnetic field, the applied field is excluded from the superconductor. It acts as a perfect diamagnet, so that the magnetic induction is zero in the interior (B=0) (Equation.2.1). Thus, if a superconductor is cooled in a magnetic field from above T_c to under the T_c, the lines of induction B are pushed out [Fig2.2(b)] of the superconcting material.

$$B = B_a + 4\pi M \tag{2.1}$$

$$\frac{M}{B_a} = \frac{-1}{4\pi} \tag{2.2}$$

$$4\pi\chi = \quad -1 \tag{2.3}$$

M is magnetization and M/B_a is magnetic susceptibility (χ) that has to be -1 when the perfect diamagnetism (Equation 2.3). Therefore, If we discovery a new type of superconductor, we have to be bothered about electrical properties and magnetic properties. Among magnetic properties, there are two types of superconductor, type-1 and type-2. These types have many in common properties but show substantial differences in their magnetic behavior that according to how the Meissner effect breakdown occurs.

Type-1 superconductors, superconductivity is abruptly destroyed through a first order phase transition when the strength of the applied field is increasing above a critical value H_c [Fig2.3(a)]. This type of superconductivity is normally exhibited by most of pure metals such as aluminum, lead and mercury.

In contrast with type-1 superconductor, type-2 superconductors occur that the formation of magnetic flux penetrate into the materials in an applied magnetic field, which is named vortex. This phenomenon takes place firstly above a certain critical field strength, which is the lower critical field, H_{c1}. And the vortex density increases as increasing field strength. At some point, superconductivity is completely destroyed that is upper critical field, H_{c2}. Between superconducting state and normal state is called the mixed state or vortex state[Fig2.3(b)], which is coexisting of superconducting state and normal state. This state is important to reveal the superconducting mechanism and alloys generally exhibit type-2 superconductor.

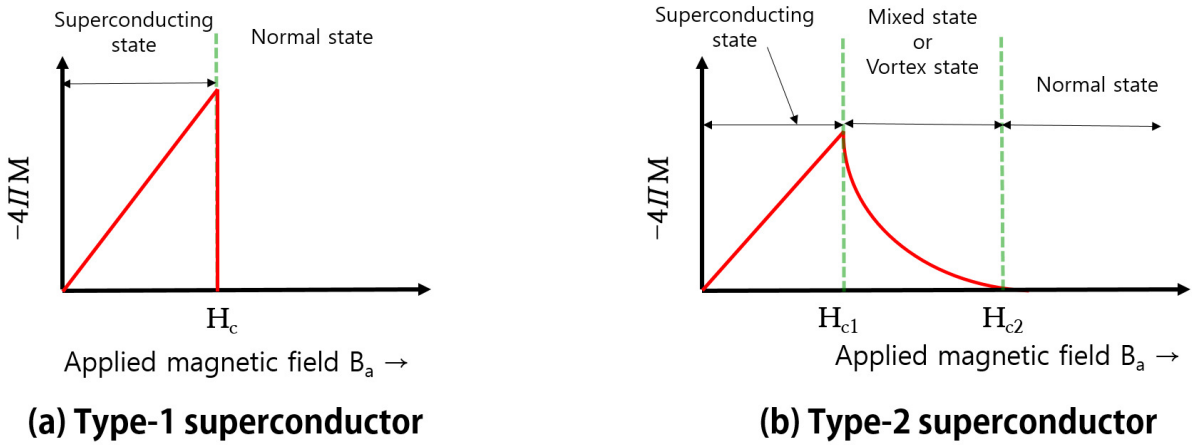

Figure 2.3: Magnetization versus applied magnetic field for (a) type-1 and (b) type-2 superconductor[15].

2.2 Bean's Critical Current Density

In 1913, H. Kamerlingh Onnes discovered first existence of critical current density (J_c), as a consequence like critical field (H_c). He figured out that there existed a threshold value of that can be carried by a superconducting sample before it reverts to its normal state. This is known as the critical current density (J_c). In other words, if the critical current density exceed its value, resistance of superconductor will occur and superconductivity will be broken simultaneously. The critical current density is related on the critical field strength and it is also an extremely important parameter in applications of superconductivity.

The critical current density can be estimated by using the magnetization hysteresis loops. A representative model is that can be used as the Bean's critical state model[16][17]. This model is introduced by Charles P. Bean in 1964. Bean's critical state model is based on that the irreversible superconductors are possible to carry a limiting superconducting current density (J_c). In order to get J_c from the magnetization hysteresis loops, this model is assumed constant J inside the sample where the magnetic field region, which

means that J_c is independent of the magnetic field. At this time, the field is applied parallel to the thickness of the sample, and J_c is proportional to the flux gradient dB/dx, as shown in [Fig2.4]

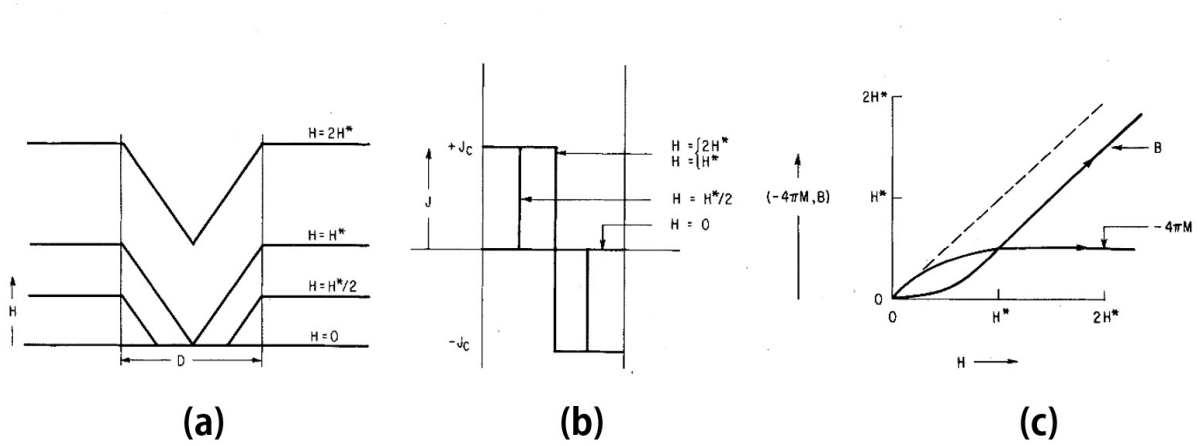

Figure 2.4: The distribution of (a) local fields and (b) current density and (c) its magnetization curves when the critical current density is independent of the magnetic field. Note that external field H = 0, $H^*/2$, H^*, and $2H^*$ is applied parallel to the surfaces lab with the superconductor of thickness D.[17].

If this Bean's critical state model is applied to the shape of a rectangular single crystal , we can obtain (equation 2.4) from the magnetization hysteresis loops [18].

$$J_c = \frac{20\Delta M}{a(1-\frac{a}{3b})} \tag{2.4}$$

Here ΔM is $(M_{down} - M_{up})$ that is the difference value of the M value at the same field, where M_{down} and M_{up} is measured by increasing and decreasing field to applied along the c axis, respectively. a and b are characteristic length of the sample widths $(a < b)$, c is the smallest dimension and the sample thickness [Fig2.5]. This (equation 2.4) is written in electromagnetic units where the magnetic moment is in emu, all lengths are in centimeter, so units of critical current density is in A/cm^2.

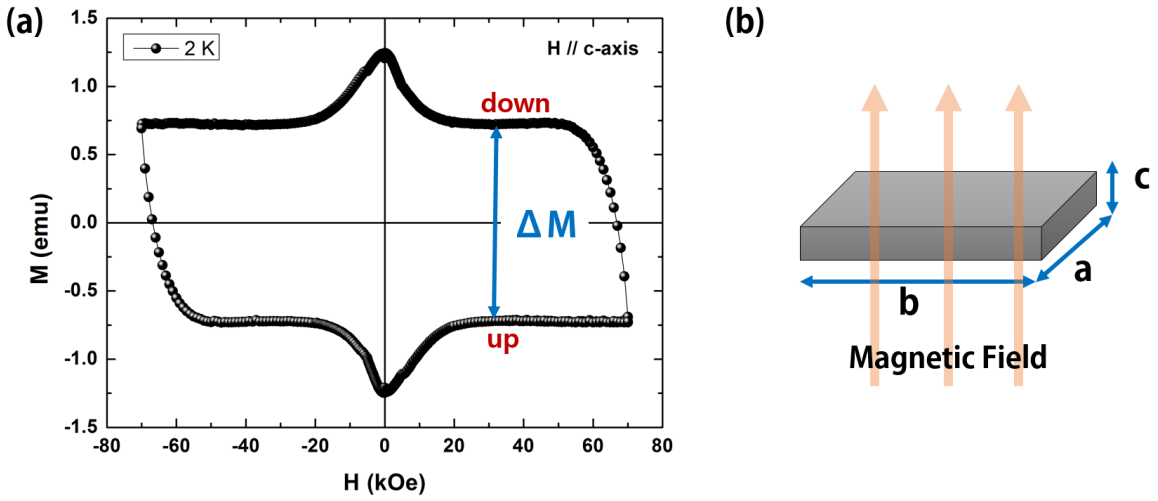

Figure 2.5: (a) Magnetization curve for $Ca_{10}Na_x(Pt_3As_8)(Fe_2As_2)_5$ at 2 K is the difference of the M value at the same field and (b) measurement of schematic.

2.3 Flux Pinning in Superconductor

Generally, the type-2 superconductors are mostly composed with alloys material, such as $NbSn_3$, MgB_2, high-Tc superconductors, and are more suitable for practical application than type-1 materials. However, type-2 superconductors generate vortex motion resulting in power losses that puts difficulty in the integration of type-2 materials in the real systems. The vortex motion is induced by the Lorentz force, $F_L = J \times B$, where J is applied current density and B is induction magnetic field proportional to the number of vortices [Fig2.6 and 2.7][19].

Yet, there is a method of preventing the vortex motion by pinning the flux in the superconductors In other words, the flux pinning works to grab the vortex so that the vortex are not able to move within superconductor. Mainly, It occurs in between superconducting region and the weak or non-superconducting region because of the energy difference. $F_L = F_p$, where $F_p = -J_c \times B$ is flux pinning force density and J_c is critical current density. Depending on the different conditions, for example the pinning size,

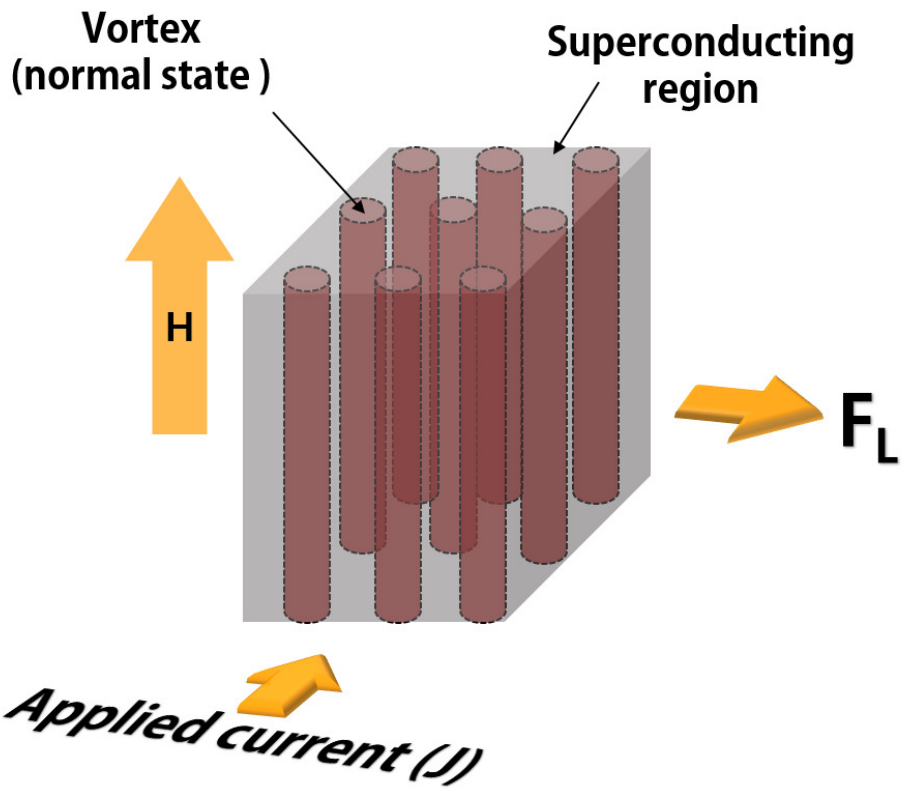

Figure 2.6: Simple schematic for flux pinning[19].

distribution and topography, the effectiveness of the flux pinning force can be decided by the flux pinning sources. Likewise, defects such as point, columnar, line, planar, etc. can act as the flux pinning centers in weak or non-superconducting regions.

In 1963, Kim [21] first mentioned the concept of flux pinning and the scaling law for the flux pinning force density as revealed by Fietz and Webb experimentally, shown as $F_p = [H_{c2}(T)]^{2.5} f(h)$, where $f(h)$ is a function of the reduced field $h(= H/H_{c2})$ [22]. The approximate scaling laws for flux pinning force is indicated in following the form.

$$F_p(h,T) = AH_{c2}^m(T)h^p(1-h)^q \tag{2.5}$$

The parameters m, p and q are dependent on the pinning mechanism, and the maximum flux pinning force density ($F_{p,max}$) is correlated with upper critical field ($H_{c2}(T)$),

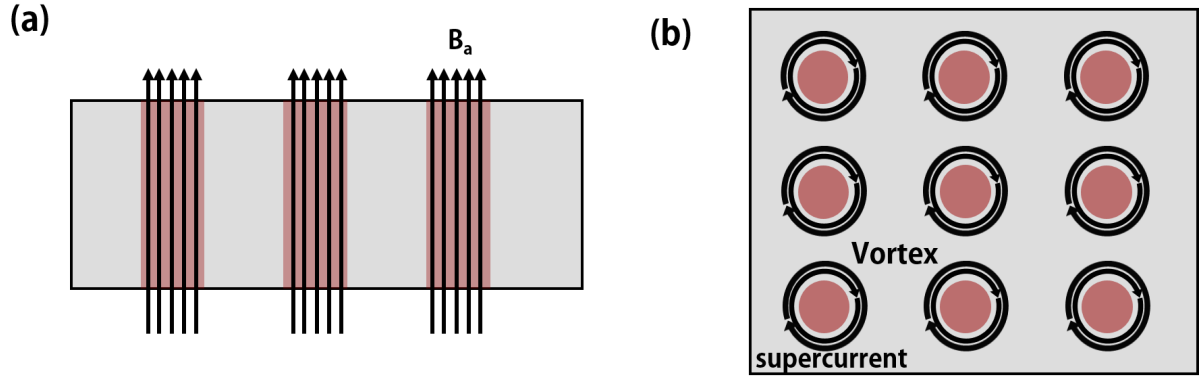

Figure 2.7: Simple schematic for flux pinning (a) side view and (b) top view, encircling supercurrent vortex[20].

as described in (equation 2.5). A number of researchers have been studied for investigating the origin of superconductor through the flux pinning mechanism. However, there are many things that should be clearly revealed for vortex phenomenon still. Basically, we try to apply the two kinds of the flux pinning models like Kramer model and Dew-Hughes model. The two models are famous in used to discover this pinning mechanism in superconductors.

2.3.1 The Kramer Model

The Kramer model is proposed on the basis of dynamic pinning force for scaling of flux pinning force [23]. Kramer was explained that when the number density of pins is sufficiently high, strains for the flux line lattice due to individual pins heavily overlap, and each flux line seems to be pinned as if by a line pin parallel to itself [24]. This is line pinning and could be expressed in the formula as (equation 2.6), where f_p is the pinning force per unit length of flux line. In other words, it defines same as an effective line pinning force $\widetilde{f_p}$.

$$\widetilde{f_p} = w f_p \tag{2.6}$$

According to Kramer model, Kramer use the results of the pinning theory, which is reported by Yamafuji and Irie [25] in order to evaluate the pinning force density. Yamafuji and Irie first introduced about pinning force(F_p), which is gained from the pinning power loss density $F_p < v >$, where $< v >$ is mean velocity at the flux-line lattice(FLL).

Kramer exhibited that the maximum flux pinning force density is $F_p(h) \propto F_s(h)$, where $F_p(h)$ is pin-breaking and $F_s(s)$ is FLL shearing dynamic pinning force. The dynamic pinning force if all pinning interactions are broken, it can be shown as (equation 2.7)

$$F_p = 2P\rho(\frac{\widetilde{f_p^4}}{(C_{66})^3})(\frac{B}{\Phi})^{0.5} \tag{2.7}$$

where P is approximately a constant, ρ is the density of strong line pins and B/Φ has been substituted for the vortex-vortex spacing of FLL, C_{66} is the shear modulus. In this case, the shear modulus C_{66} is applied for high-field superconductors. As to the magnetic field dependence, (equation 2.7) leas to (equation 2.8) except for the low magnetic field region.

$$F_p = \frac{K_p h^{0.5}}{(1-h)^2} \tag{2.8}$$

Where, $h = H/H_{irr}$ and K_p is a constant dependent on the temperature and its temperature dependence is by $K_p \propto H_{c2}^{2.5}$. Hence, the pinning force density increases with increasing magnetic field caused by the synchronization. In case of $F_p(h)$, the dynamic pinning force assumed that all pins are broken, while the FLL shearing dynamic pinning force density $F_s(h)$ is derived from the plastic shear of the FLL around strong line pins rather than elastic deformation because the line pins are too strong to be broken. So, the FLL shearing dynamic pinning force can be expressed as (equation 2.9)

$$F_s(h) = K_s h^{0.5}(1-h)^2 \tag{2.9}$$

where K_s also is proportional $H_{c2}^{2.5}$ and we called the Kramer's formula. Using this Kramer's formula, the H_{c2} can be estimated and (equation 2.9) reduces to

$$F_p = J_c B \qquad F_p^{0.5} B^{-0.25} = J_c^{0.5} B^{0.25} \quad \propto \quad K_s^{0.5} h^{0.25} B^{-0.25}(1-h) \tag{2.10}$$

$$K_s \quad \propto \quad H_{c2}^{2.5} \qquad F_p^{0.5} B^{-0.25} \quad \propto \quad H_{c2}(1 - H/H_{c2}) \tag{2.11}$$

$$J_c^{0.5} B^{0.25} \quad \propto \quad (H_{c2} - H) \tag{2.12}$$

and consequently, by extrapolating the linear part of the experimental data on $J_c^{0.5} B^{0.25}$ versus H.

2.3.2 Dew-Hughes Model

Dew-Hughes model is a little bit different from Kramer's model. Dew-Hughes supposed that flux-pinning is able to predict the various observed forms of $f_n(h)$, according to the details of the pinning processes[26]. He proposed about an occurrence of the shearing flow of flux lines, and the morphology of the pin is important to determine the resultant pinning characteristic. Based on this thinking, He suggested that related to interact between individual flux-lines and pinning centers, and the geometry of the pinning centers for the effect on flux pinning mechanism. Moreover, he described different flux pinning behavior in the two kinds of superconductors, NbTi and $NbSn_3$ depending upon the morphology of the boundary structure [Fig2.8][27].

The pinning force per unit volume is given by (equation 2.13),

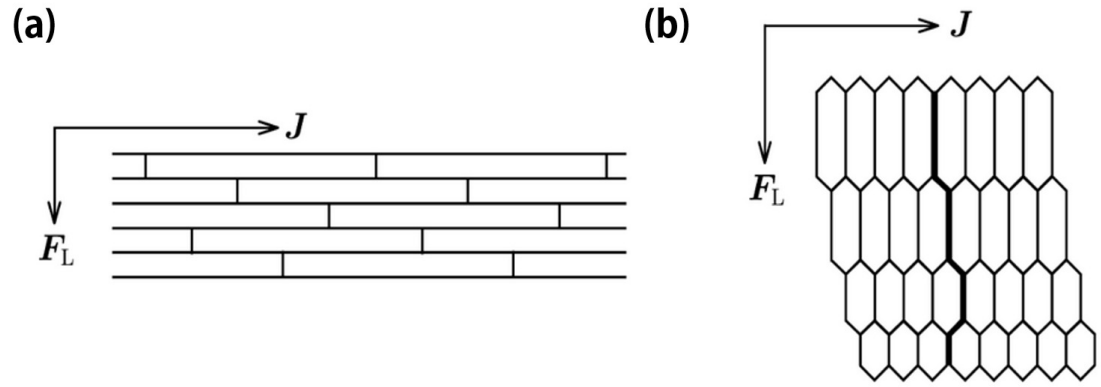

Figure 2.8: Simple diagrams of the morphology of pins to explain the model of Dew-Hughes in (a) NbTi and (b) Nb_3Sn. J is current and F_L is the Lorentz force.[28].

$$F_p = \eta L f_p = \frac{-\eta L \Delta W}{x} \tag{2.13}$$

Where η is an efficiency factor determined by elasticity of the flux lattice, L is the total length of the flux-line per unit volume, and f_p is the pinning force per unit length of the pinned vortex, which could be express by $-\Delta W/x$. ΔW indicate the work done in moving unit length of the flux-line from a pinning center to the nearest position where it is unpinned and x is the effective range of the pinning interaction[26]. The efficiency factor would be skipped, if the case of strong pins in the elasticity effect of the FLL is neglected and the other parameters will be defined depending on the situation in (equation 2.13). In [table 2.1] are summarized that flux-pinning function and its connected with the parameters according to the specific situations. In addition, graph of flux pinning function made by following the [table 2.1], are shown as [Fig2.9]. As shown in [table 2.1] and [Fig2.9], the pinning function $F_p(h)$ is varied sensitively according to parameters of p and q. Furthermore, the value of H_{c2} is need to be carefully confirmed because the shape of the pinning function changes depending on H_{c2}. Thus, these induced various F_p(h) means that can be defined as the geometry of pin such as point, surface, and volume pins,

according to the peak positions(h_{max}) of F_p(h) and the shape of F_p(h).

Type of interaction	Geometry of pin	L	x	Type of centre	ΔW	$F_p(h)$	h_{max}
Magnetic	**Volume**	$\frac{S_v}{d}$	λ	**Normal**	$\frac{-\phi_0(H_{c2}-H)}{2.32\kappa^2}$	$\frac{\mu_0 S_v H_{c2}^2 h^{0.5}(1-h)}{\kappa^3}$	$h = 0.33$
				$\Delta\boldsymbol{\kappa}$	$\frac{-\phi_0(H_{c2}-2H)\Delta\boldsymbol{\kappa}}{2.32\kappa^3}$	$\frac{\mu_0 S_v H_{c2}^2 h^{0.5}(1-2h)\Delta\boldsymbol{\kappa}}{\kappa^4}$	$h = 0.17{,}1$
Core	**Volume**	$\frac{S_v}{d}$	d	**Normal**	$\frac{-\mu_0\phi_0(H_{c2}-H)^2}{4.64\kappa^2\boldsymbol{B}}$	$\frac{\mu_0 S_v H_{c2}^2 (1-h)^2}{5.34\kappa^2}$	-
				$\Delta\boldsymbol{\kappa}$	$\frac{-\phi_0(H_{c2}-2H)\Delta\boldsymbol{\kappa}}{2.32\kappa^3}$	$\frac{\mu_0 S_v H_{c2}^2 h\,(1-h)\Delta\boldsymbol{\kappa}}{2.67\kappa^3}$	$h = 0.5$
	Surface	$\frac{S_v}{d}$	ξ	**Normal**	$\frac{-\pi\xi^2\mu_0(H_{c2}-H)^2}{4.64\kappa^2}$	$\frac{\mu_0 S_v H_{c2}^2 h^{0.5}(1-h)^2}{4\kappa^2}$	$h = 0.2$
				$\Delta\boldsymbol{\kappa}$	$\frac{-\pi\xi^2\mu_0 H(H_{c2}-H)^2\Delta\boldsymbol{\kappa}}{2.32\kappa^3}$	$\frac{\mu_0 S_v H_{c2}^2 h^{1.5}(1-h)\Delta\boldsymbol{\kappa}}{2\kappa^3}$	$h = 0.6$
	Point	$\frac{BV_f}{\emptyset_0}$	$\frac{a}{2}$	**Normal**	$\frac{-\pi\xi^2\mu_0(H_{c2}-H)^2}{4.64\kappa^2}$	$\frac{\mu_0 V_f H_{c2}^2 h(1-h)^2}{4.64a\kappa^2}$	$h = 0.33$
				$\Delta\boldsymbol{\kappa}$	$\frac{-\pi\xi^2\mu_0 H(H_{c2}-H)^2\Delta\boldsymbol{\kappa}}{2.32\kappa^3}$	$\frac{\mu_0 V_f H_{c2}^2 h^2(1-h)\Delta\boldsymbol{\kappa}}{2.32a\kappa^3}$	$h = 0.67$

Table 2.1: Summarized flux pinning functions for specific situations[26].

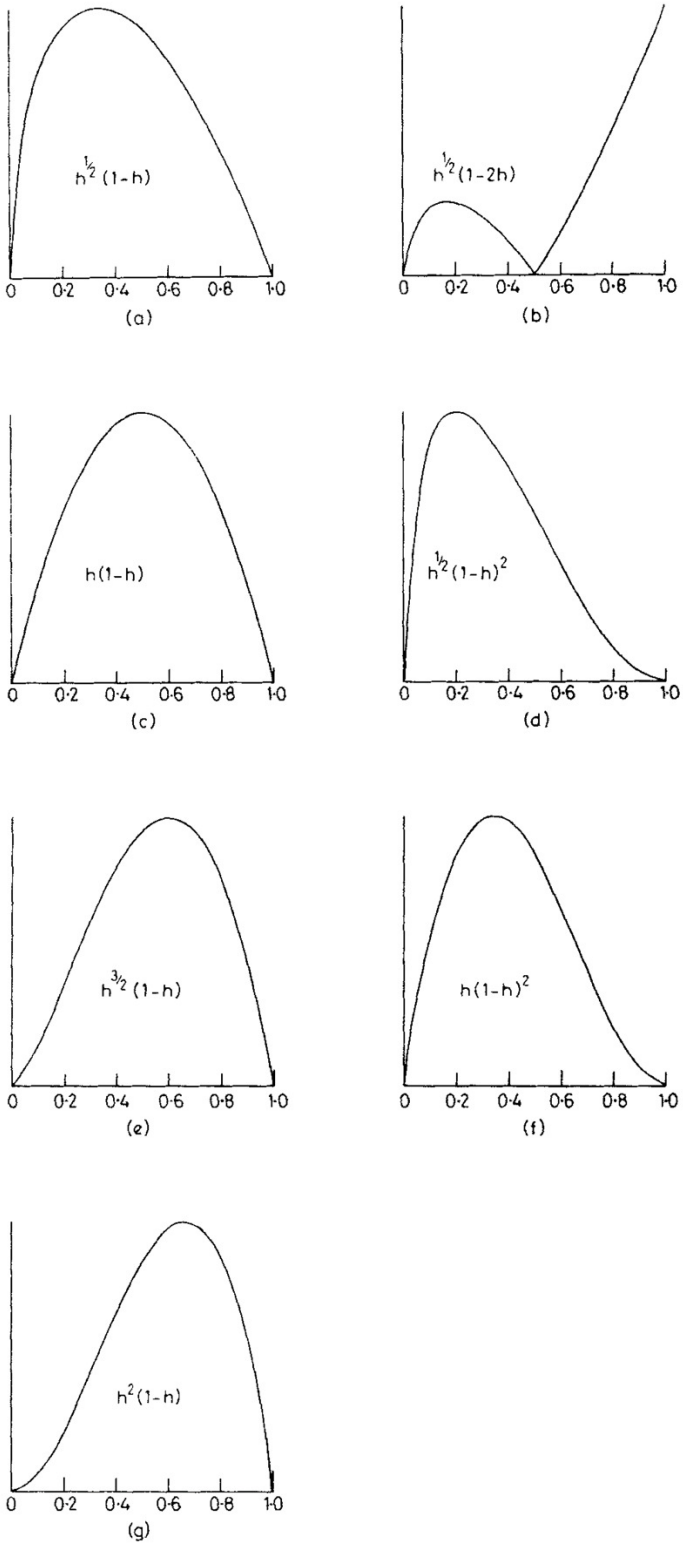

Figure 2.9: flux pinning force density versus h for the various expressions given in table2.1[26].

Chapter 3. Growth of Single Crystal

There are several methods such as Czochralski, Bridgman, Floating zone methods and high temperature solution growth that can be used to grow single crystal. Among these methods, Bridgman method is one of the oldest and well known techniques used for growing crystals.

3.1 The Birdgman Method

Bridgman method controls the crystallizing point using a temperature gradient in a furnace[29]. The crucible containing the molten material is translated slowly downward into the cold zone along the axis of a temperature gradient [Fig3.1]. The temperature at

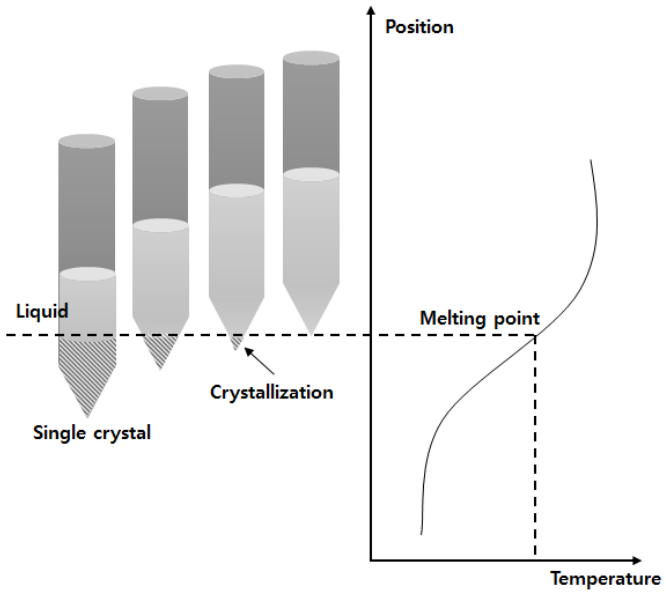

Figure 3.1: Schematics of crystal growth by a Bridgman method[30]

the bottom of the crucible is kept at below the solidification temperature, and the crystal growth is initiated by the seed at the melt-seed interface. This method has an advantage

to grow large crystals. Therefore, Bridgman method was employed to grow iron based superconductors in the present study.

3.2 Quartz tube manufacturing

Iron-based superconductors include a strong volatile elements such as As, P, Se, and S. The constituent elements have characteristic of high vapor pressure, so usually should be prereact in a vacuum sealed quartz tube or Alumina tube before encapsulating in a refractory metal crucible to prevent from evaporation during welding of crucible in vacuum by electron beam welder. After being shaped from the quartz tubes in [Fig3.2] by an oxygen-hydrogen torch, we should wash the quartz tube cleanly to prevent impurities from getting in the quart tube. The way of creating quartz tubes was summarized in a below[31].

1. Cut off the quartz tubes 50 cm using a circular saw.
2. Cutting quartz tubes were divided into two parts by a oxygen-hydrogen torch.
3. Etched for 1 minutes with a HF.
4. Washed with deionized water in two times
5. We are dried to remove residue of H_2O in oven.

3.3 $FeAs_{1.175}$ Precursor

According to reference[32], Arsenic (As) has high vapor pressure, so we already made precursors, $FeAs_{1.175}$. As was added 1.175 mole ratio because vapor pressure is about 100

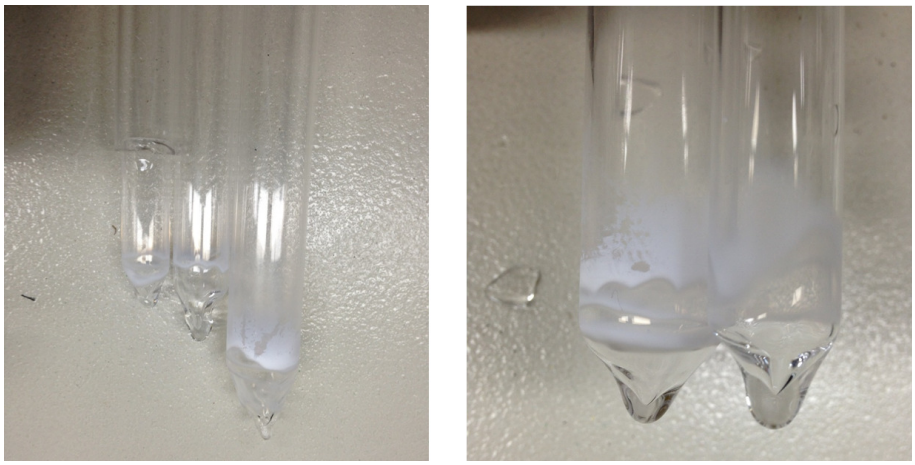

Figure 3.2: Quartz tubes created by oxygen-hydrogen torch

kPa at 600 °C. So, we prepared pre-reaction of precursor, which is approximately 10 g of $FeAs_{1.175}$ by a solid reaction.

The mole ratio mass of Iron (Fe) powder (99.9 %) and As lumps (99.999%) are weighted on a balance with the accuracy of 0.001 g. After that, these material put in the quartz tube and are sealed under vacuum (10^{-6} torr) by an oxygen-hydrogen torch. As shown in [Fig3.3(a)], the furnace was heated to 1050 °C slowly at a rate of 8 °C/h and kept at that temperature for 40 hours. And then, the furnace was cooled to room temperature at a rate of 100 °C/h over 8 hours [Fig3.3(b)][33]. Approximately 10 g of $FeAs_{1.175}$ precursor was prepared by a solid reaction.

3.4 Growth of the $Ca_{10}Na_x(Pt_3As_8)(Fe_2As_2)_5$ Single Crystal

Single crystalline $Ca_{10}Na_x(Pt_3As_8)(Fe_2As_2)_5$ was grown by the closed Bridgman method with a molybdenum (Mo) crucible [Fig3.4]. Mo crucible is properly for growth of single crystalin high temperature. Because crucible should be used satisfy following the conditions, very small reaction with the sample at high temperature and mechanically

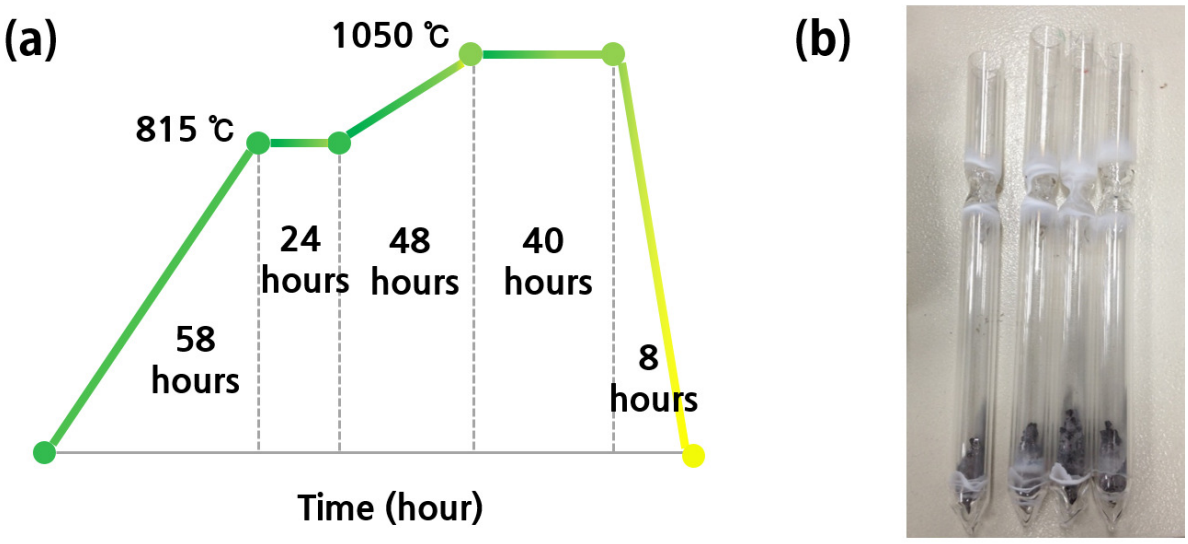

Figure 3.3: (a)Sequence of precursor $FeAs_{1.175}$ and (b) reacted precursor $FeAs_{1.175}$ in a box furnace.

easy processing. Therefore, the melting point of Mo is 2610 °C, its proper temperature. Moreover Mo rod is cheap and easy to process. We also use a closed Bridgman method. To prevent the constituent elements from evaporation, the molybdenum crucible is welded with the covering cap under Ar atmosphere by an arc melting[Fig 3.6and 3.5].

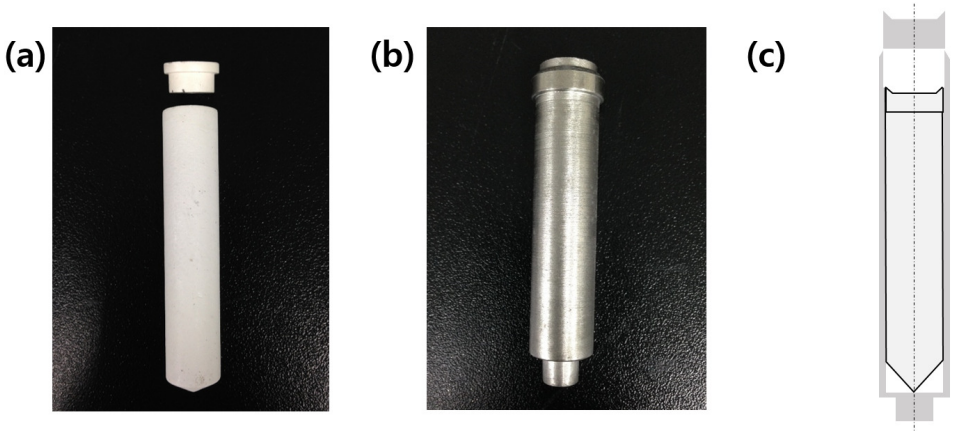

Figure 3.4: (a) BN crucible (b) Mo crucible (c) crucible projection drawing

The vacuum furnace with tungsten heather is used to grow a single crystal from a high melting point. It is very convenient and has an excellent stability of the temperature below 2000 °C. The crucible is vertically moved by the external force in Bridgman

Figure 3.5: Welding process and crucible after arc welding

method. The construction of this furnace is shown in [Fig 3.7(a)].

$Ca_{10}Na_x(Pt_3As_8)(Fe_2As_2)_5$ single crystal was synthesized with nominal composition ratio. We used to already pre-reacted precursor of $FeAs_{1.175}$ and added 4 moles of Sodium (cubic pieces), 8 moles of Calcium (dendritic pieces, 99.99 %), 3.3 moles of Platinum (wire, 99.999 %) and 8.3 moles of As (lumps, 99.99 %). First, precursor of $FeAs_{1.175}$ placed into the ground of pyrolytic boron nitride (PBN) crucible [Fig3.4], to avoid the reaction between precursor and Molybdenum crucible. After that, the rest of material put in a PBN crucible in according to the high vapor pressure before inserting into a Mo crucible.And then, the cap of the crucible must be welded by the arc welder as soon as possible.

The welded crucible was located in a vacuum furnace with a tungsten mesh heater and heated slowly to 1550 °C though 17 hours period. When the temperature arrived at 1550 °C and held at that position for 12 hours, and then it moved slowly downward from

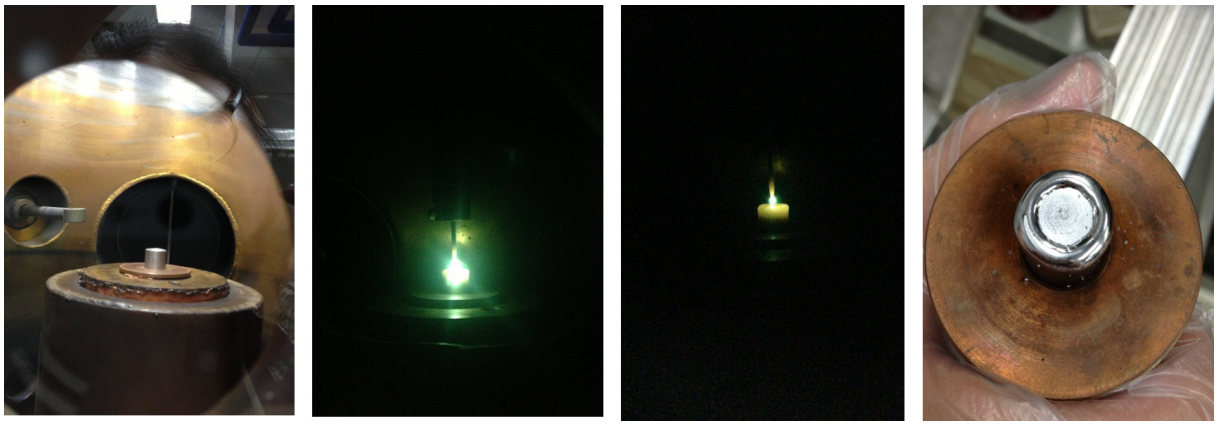

Figure 3.6: Arc welding system

the tungsten mesh heater in the vacuum furnace over 100 hours at a rate of 1.6 mm/h [Fig 3.7(b)]. A grown $Ca_{10}Na_x(Pt_3As_8)(Fe_2As_2)_5$ single crystal by a closed Bridgman method is cut to suitable size for each experiment. But, this crystal piece including sodium is easy to oxidize under air and H_2O. So, to obtain accurate results, we always have to prepare to measure in the glove bag filled with Ar gas.

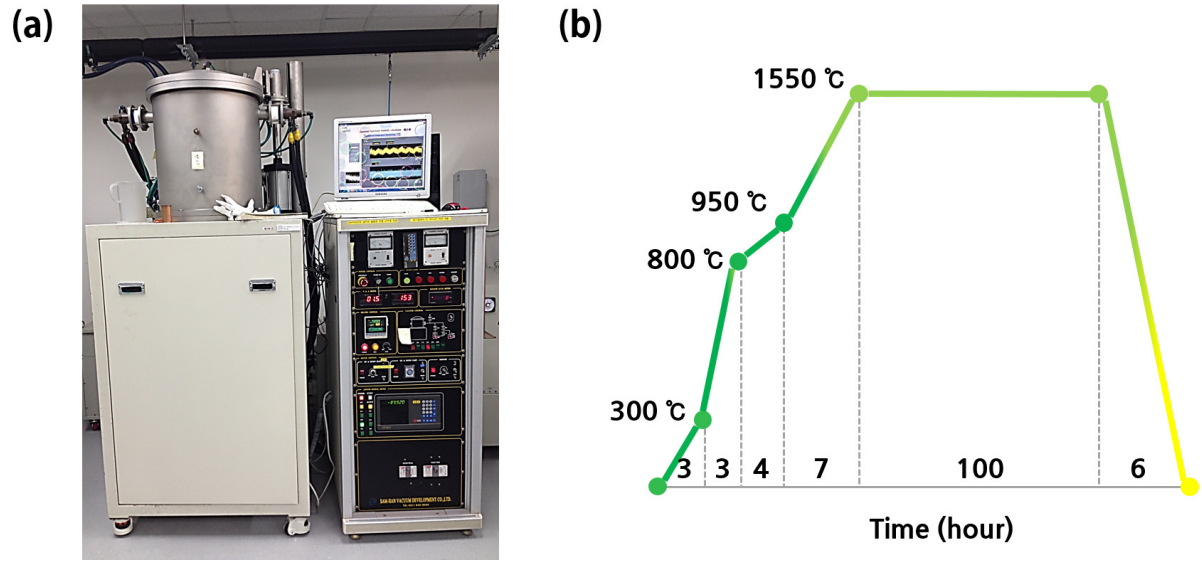

Figure 3.7: (a) The vacuum furnace and (b) sequence of $Ca_{10}Na_x(Pt_3As_8)(Fe_2As_2)_5$ single crystal

Chapter 4. Experimental Method

Temperature dependence of resistivity for the prepared superconductor was measured by Physical Property Measurement System (PPMS) and Magnetic Property Measurement System (MPMS) was used to obtaining critical current density. For the rest, a crystallographic axis for the prepared superconductor was checked by X-ray Powder Diffraction (XRD) and Scanning Electron Microscopy (SEM), respectively.

4.1 X-ray Diffraction (XRD) and Scanning Electromicroscope (SEM)

Figure 4.1: X-ray diffractometer (Empyrean PANalytical) in DGIST Fab.

The single crystal structure of the $Ca_{10}Na_x(Pt_3As_8)(Fe_2As_2)_5$ was examined by X-ray diffractometer (Empyrean PANalytical)[Fig4.1] used Cu $K_{\alpha 1}$ source. The single crystal of $Ca_{10}Na_x(Pt_3As_8)(Fe_2As_2)_5$ was carefully ground in the glove bag filled

with Ar gas. The powder X-Ray Diffraction (XRD) took approximately 1 hour. After then, the lattice constants were done by Rietveld refinement through the software program, HighScore Plus, provided by PANalytical. To identify the composition ratio, the $Ca_{10}Na_x(Pt_3As_8)(Fe_2As_2)_5$ was analyzed by a field emission scanning electronmicroscope (FE-SEM)(Hitachi S-4800) and we observed the surface of the sample. Scanning Electron Microscope (SEM) was used to confirm the image of the atomic surface and the atomic percentage of the single crystal. SEM is incident into the sample by the electron beam generated by the electron gun. At this time, a back-scattered electron or secondary electron is emitted. This detected electron is observed and analyzed on the surface of the sample. Additionally, it is possible to examine the atomic percentage ratio using Energy Dispersive x-ray Spectroscopy (EDS).

4.2 Transport Property Measurement

The resistivity measurement was carried out on a Physical Property Measurement System (PPMS) manufactured by Quantum Design. This equipment is availed to measure the sample with magnetic fields up to 9 T between 1.9 to 400 K. In case that $Ca_{10}Na_x(Pt_3As_8)(Fe_2As_2)_5$ single crystal has the low resistance, the samples were measured in the four-point probe method. The advantage of the four-point probe method over the two-point probe method is that it largely eliminates contact resistance. The electrical resistivity measurement was measured by the standard fourpoint probe method with silver epoxy, which includes grains of silver using PPMS. It serves to lower the contact resistance between the sample and terminal as well as strengthen the adhesion between the terminal and the sample. When superconductor measures electrical resistivity, we make frequent use of the four-probe method [Fig4.2(a)]. Compared to the two-probe method,

the four-probe method minimizes the contact resistance and it is possible to eliminate probe resistance. We performed alternately the current flowing into the forward direction and reverse the direction to eliminate thermoelectromotive force caused by the contact resistance during the electrical resistivity measurement. $Ca_{10}Na_x(Pt_3As_8)(Fe_2As_2)_5$ single crystal for the four-probe technique resistance measurements was mounted on standard PPMS sample pucks [Fig4.2(b)][34].

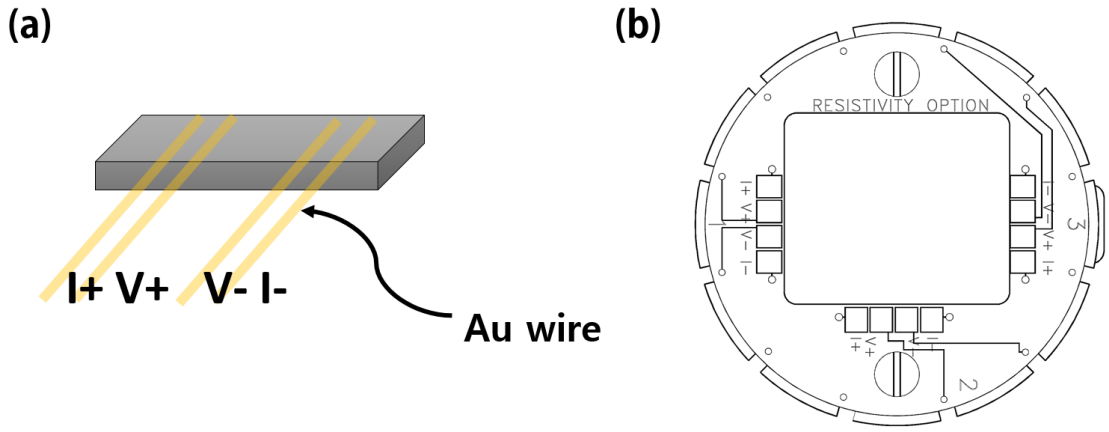

Figure 4.2: Interface on resistivity (a) four-point probe method and (b) sample puck in PPMS[34].

4.3 Magnetic Property Measurement

Magnetic properties, such as magnetization and magnetic susceptibility were conducted in Magnetic Property Measurement System Superconducting QUantum Interference Device Vibrating Sample Magnetometer (MPMS SQUID-VSM) made by Quantum Design which is shown in the picture of [Fig4.3(a)] and was actually used for this experiment. We utilized MPMS SQUID-VSM, which is a superconducting magnet giving the samples to magnetic fields up to 7 Tesla, providing temperature control of samples between 400 to 1.8 Kelvin with quartz holder[Fig4.3(b)]. This MPMS was integrated

with SQUID, a precision temperature control within a high-field superconducting magnet, and a sophisticated computer operating system. The basic principles of MPMS is accomplished by oscillating the sample near a detection coil and detecting synchronously the voltage induction. By adding the SQUID-VSM device the accuracy of measurements is further increased and the speed is faster than one with the previous model.

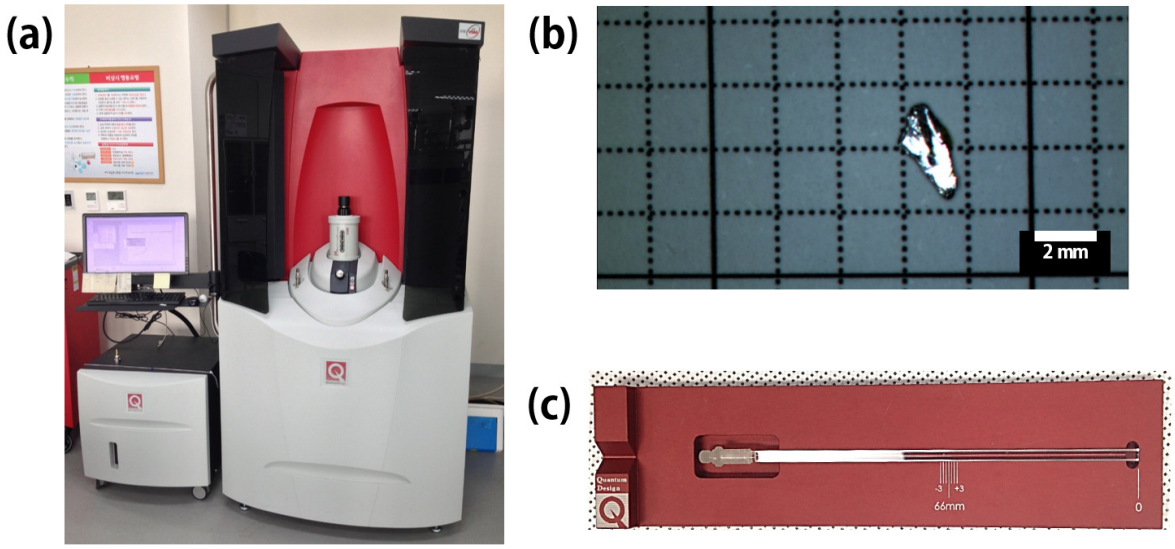

Figure 4.3: (a) Magnetic property measurement system (SQUID-VSM), (b) the single crystal of $Ca_{10}Na_x(Pt_3As_8)(Fe_2As_2)_5$ and (c) quartz holder used in SQUID-VSM.

Chapter 5. Result and Discussion

$Ca_{10}Na_x(Pt_3As_8)(Fe_2As_2)_5$ was characterized by the powder X-ray Diffraction(XRD) with Cu $K_{\alpha 1}$ radiation. [Fig5.1] shows XRD pattern for $Ca_{10}Na_x(Pt_3As_8)(Fe_2As_2)_5$ on room temperature. The XRD pattern of $Ca_{10}Na_x(Pt_3As_8)(Fe_2As_2)_5$ could be fitted with a single phase. Rietveld refinements of the data were performed with HighScore Plus, and shown in red line of [Fig5.1]. In the result of fitted results, this crystal has a triclinic unit cell with lattice constant a=8.800$\mathring{A}$, b=8.730$\mathring{A}$, c=10.945$\mathring{A}$. Lattice constant of c=10.945$\mathring{A}$ is slightly longer than the $Ca_{10}(Pt_3As_8)(Fe_2As_2)_5$ parent[35]. However, the refinements of XRD pattern could not be exactly identified in the crystal structure determination. We just expected that sodium was intercalated in $Ca_{10}Na_x(Pt_3As_8)(Fe_2As_2)_5$, following the fitted result.

The surface image, phase and atomic composition of the single crystal were checked by a Field Emission-Scanning Electron Microscopy (FE-SEM), shown in [Fig5.2]. [Fig5.2] is different magnification, whose scale refers to the bottom of image. In addition, [Fig5.2] also shows the surface of single crystals, showing one phase. [table5.1] shows the Energy Dispersion X-ray Spectroscopy (EDS) result, the atomic percentage ratio of the single crystal, which confirmed that the sample is fabricated by the elements of Ca, Na, Pt, Fe and As. [table5.1] indicates that the atomic composition ratio was analyzed.

[Fig5.3] shows resistivity versus temperature to obtain the transition temperature for the $Ca_{10}Na_x(Pt_3As_8)(Fe_2As_2)_5$. The inserted figure in [Fig5.3] is a magnified view near the superconducting transition temperature. We can observe the transition temperature. The T_c onset was 38.01 K and the T_c offset was 37.31 K. This sample indicates a narrow

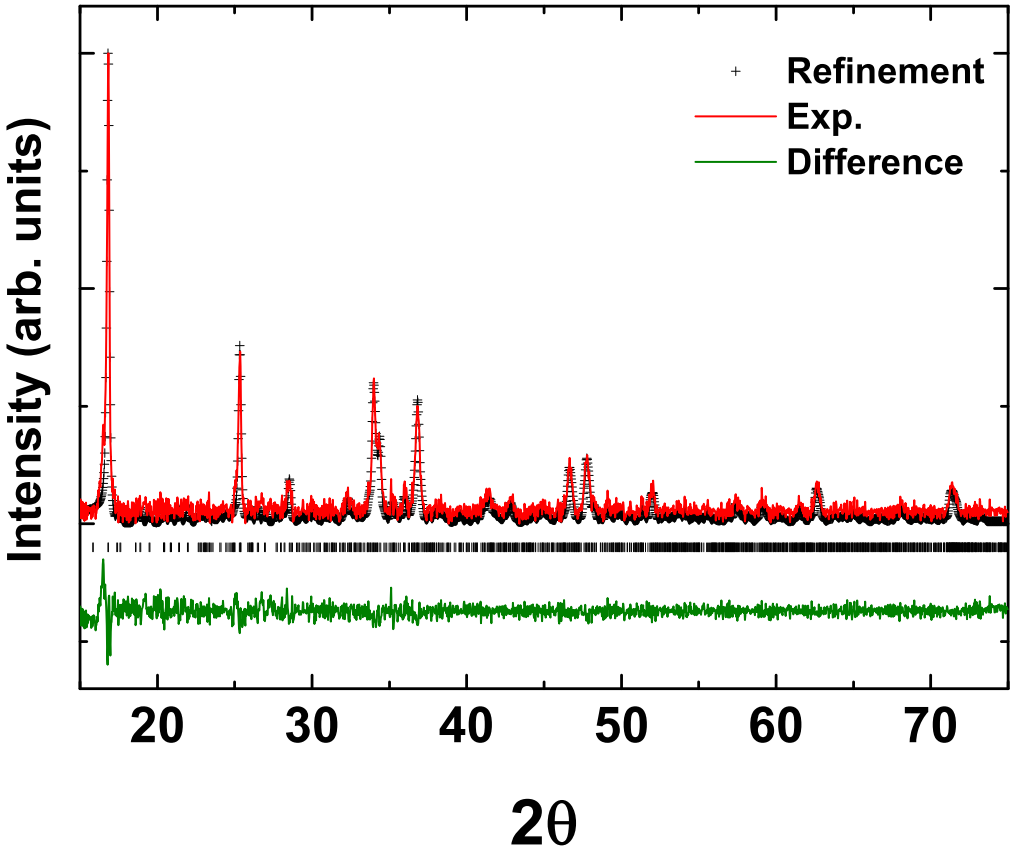

Figure 5.1: X-ray diffraction pattern and Rietveld fit of $Ca_{10}Na_x(Pt_3As_8)(Fe_2As_2)_5$ single crystal

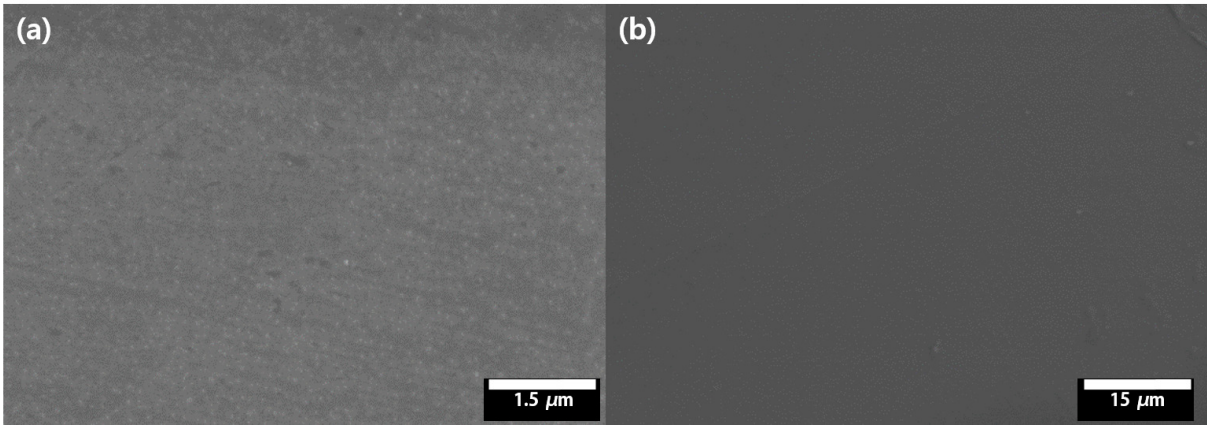

Figure 5.2: SEM image of the $Ca_{10}Na_x(Pt_3As_8)(Fe_2As_2)_5$ single crystal.

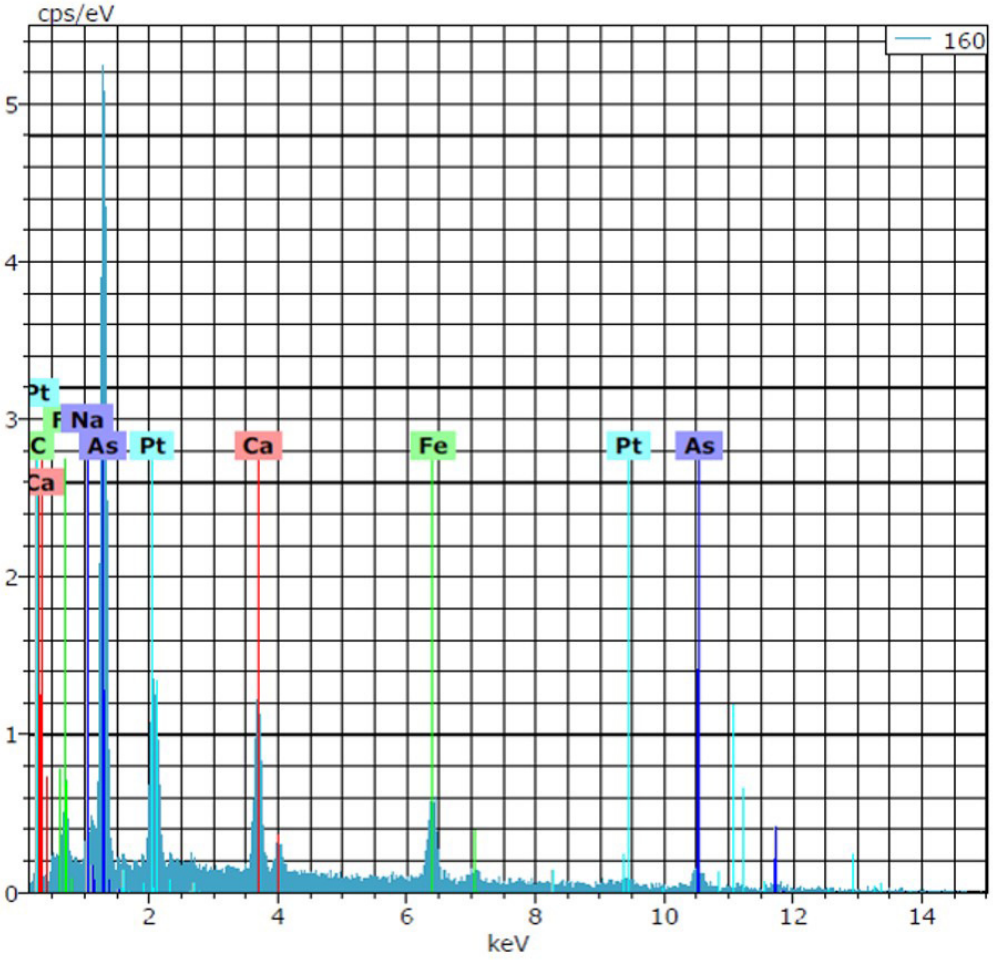

	Atomic percent	Ca reference ratio
C	39.6800	-
Na	1.7000	1.1765
Ca	14.4500	10.0000
Fe	14.3200	9.9100
As	25.3900	17.5709
Pt	4.4600	3.0865
total	100.0000	

Table 5.1: The result of EDS.

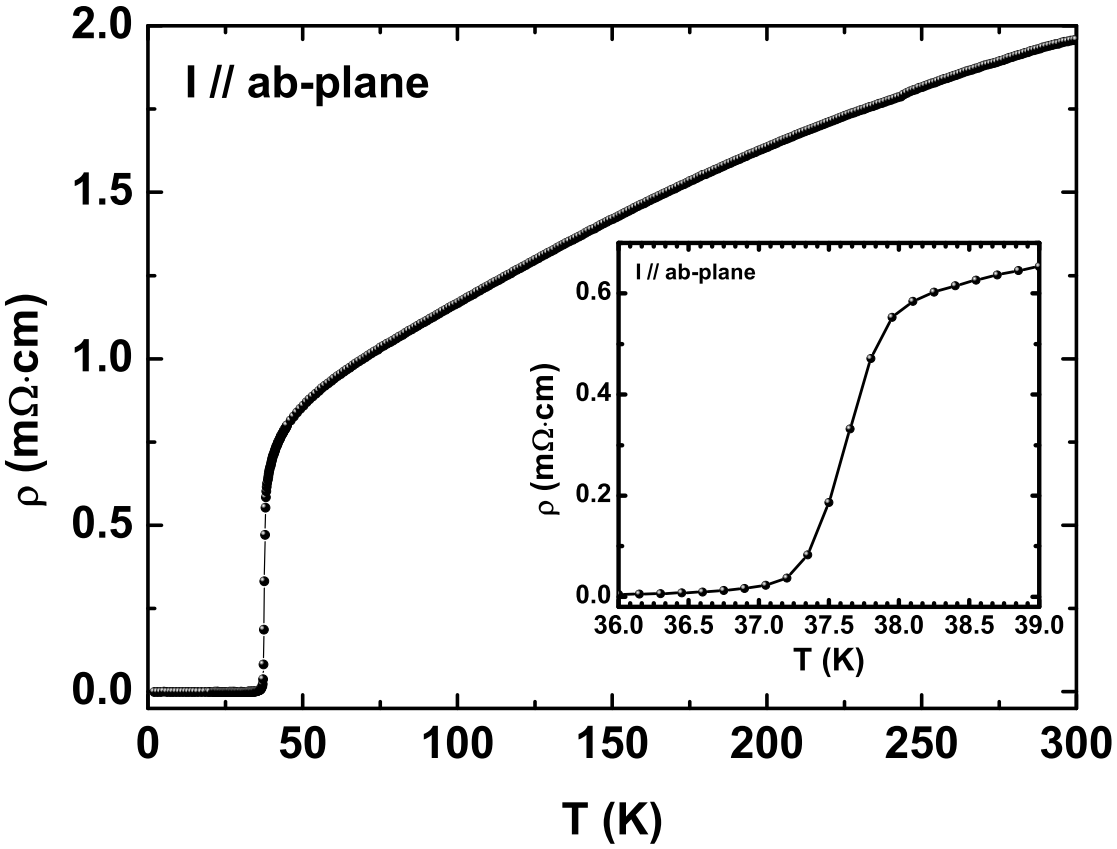

Figure 5.3: Resistivity versus temperature for $Ca_{10}Na_x(Pt_3As_8)(Fe_2As_2)_5$

superconducting transition width, about 0.7 K. This means that quality of single crystal is good and homogeneous. In addition, the residual resistivity ratio (RRR) is 3.097, The RRR value is slightly low because we assume that sodium acts as a defect in this sample.

[Fig5.4] shows the temperature dependent on magnetic susceptibility for $Ca_{10}Na_x(Pt_3As_8)(Fe_2As_2)_5$ by using QD VSM MPMS. [Fig5.4] was measured in both the zero-field-cooled (ZFC) and field-cool (FC) processes at 20 Oe with field parallel c-axis (H//c-axis). The inserted figure in [Fig5.4] is a magnified view near the onset superconducting transition temperature. In this curve, the onset superconducting transition temperature is observed at 37.07 K and the susceptibility is slowly reduced over a wide temperature range. Generally, high quality single crystal shown rapidly decreasing near transition temperature and perfect diamagnetism. On the other hand, [Fig5.4] was not indicated like perfect diamagnetism[36][37]. Besides, this result is not consistent in resistivity versus temperature. By the way, this region is a vortex state in the $Ca_{10}Na_x(Pt_3As_8)(Fe_2As_2)_5$. So, we need to study more about magnetic properties in the next part.

[Fig5.5] shows Magnetization hysteresis loop for $Ca_{10}Na_x(Pt_3As_8)(Fe_2As_2)_5$ measured by 2 K for fields up to 7 T, applied parallel in the c-axis. And the field dependent on magnetization takes at the temperature from 3 to 38 K with an interval of 2 K for fields up to 7 T shown in [Fig5.6]. Particularly in between 20 to 30 K, the second magnetization peak (SMP), called fish-tail effect, can be clearly observed [Fig5.7]. We find out similar fish-tail effect in several different crystals from Iron-based superconductor (IBSs)[39][36][37][38]. For example, in superconducting $BaFe_2As_2$ single crystal, which Cobalt(Co) and Potassium(K) are doped and the fish-tail effect is shown similar to our sample[38][40][41]. Therefore it is noteworthy compared with other IBSs because it was discovered for the first time in the $Ca_{10}Na_x(Pt_3As_8)(Fe_2As_2)_5$.

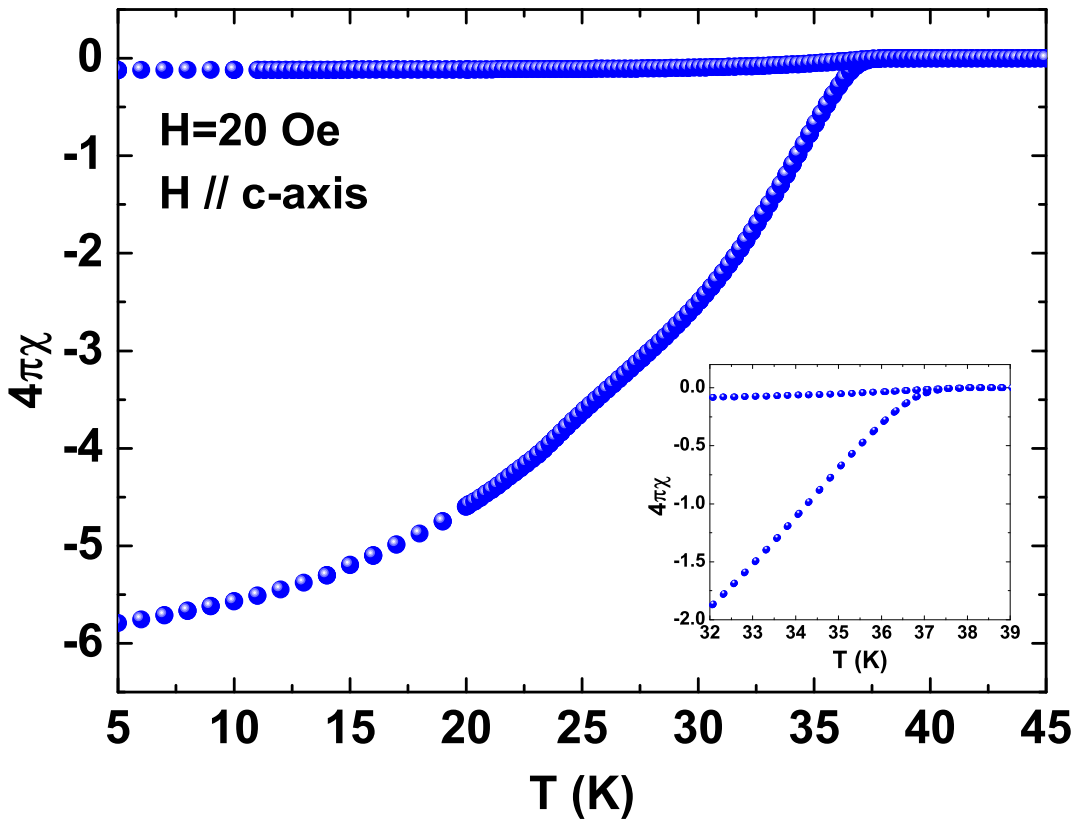

Figure 5.4: The magnetic susceptibility of the $Ca_{10}Na_x(Pt_3As_8)(Fe_2As_2)_5$ single crystal. Inset figure was enlarged at near the superconducting transition temperature.

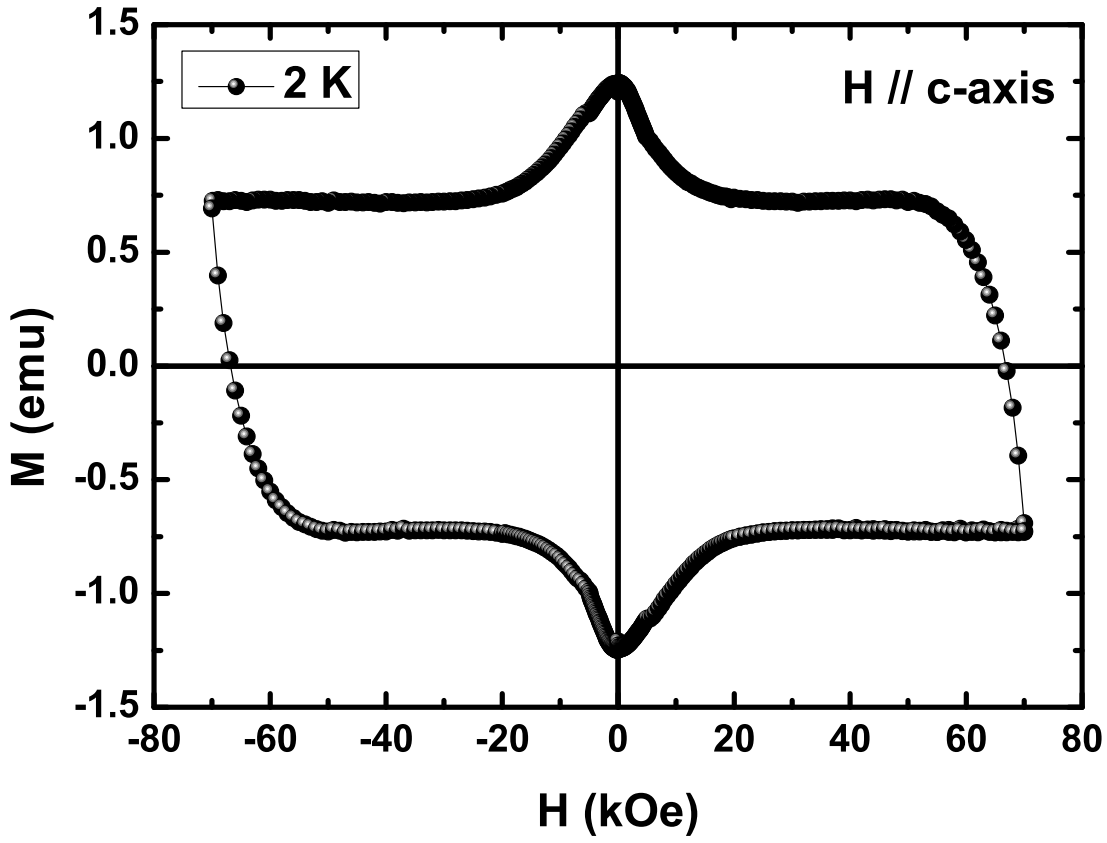

Figure 5.5: Magnetization hysteresis loop for $Ca_{10}Na_x(Pt_3As_8)(Fe_2As_2)_5$ at 2 K.

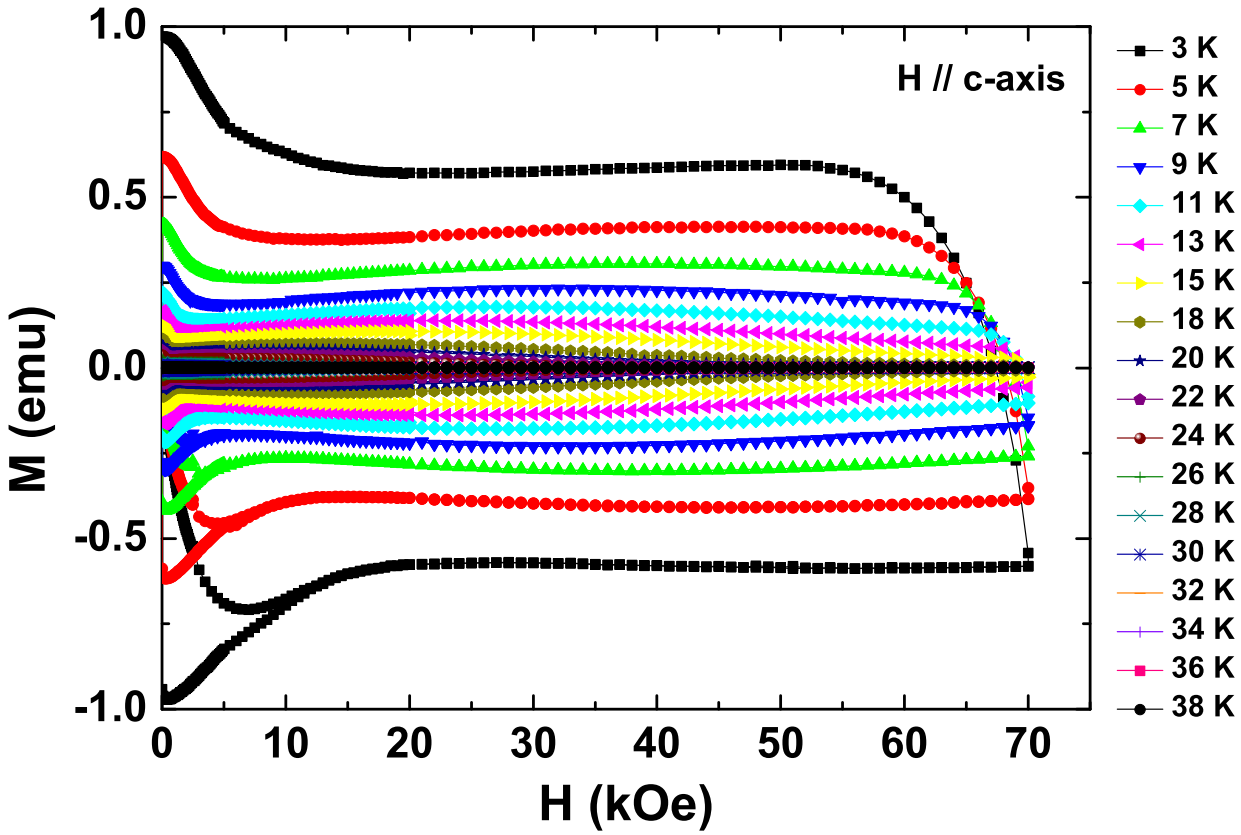

Figure 5.6: The field dependent magnetization taken at the temperature from 3 to 38 K with an interval of 2 K for $Ca_{10}Na_x(Pt_3As_8)(Fe_2As_2)_5$

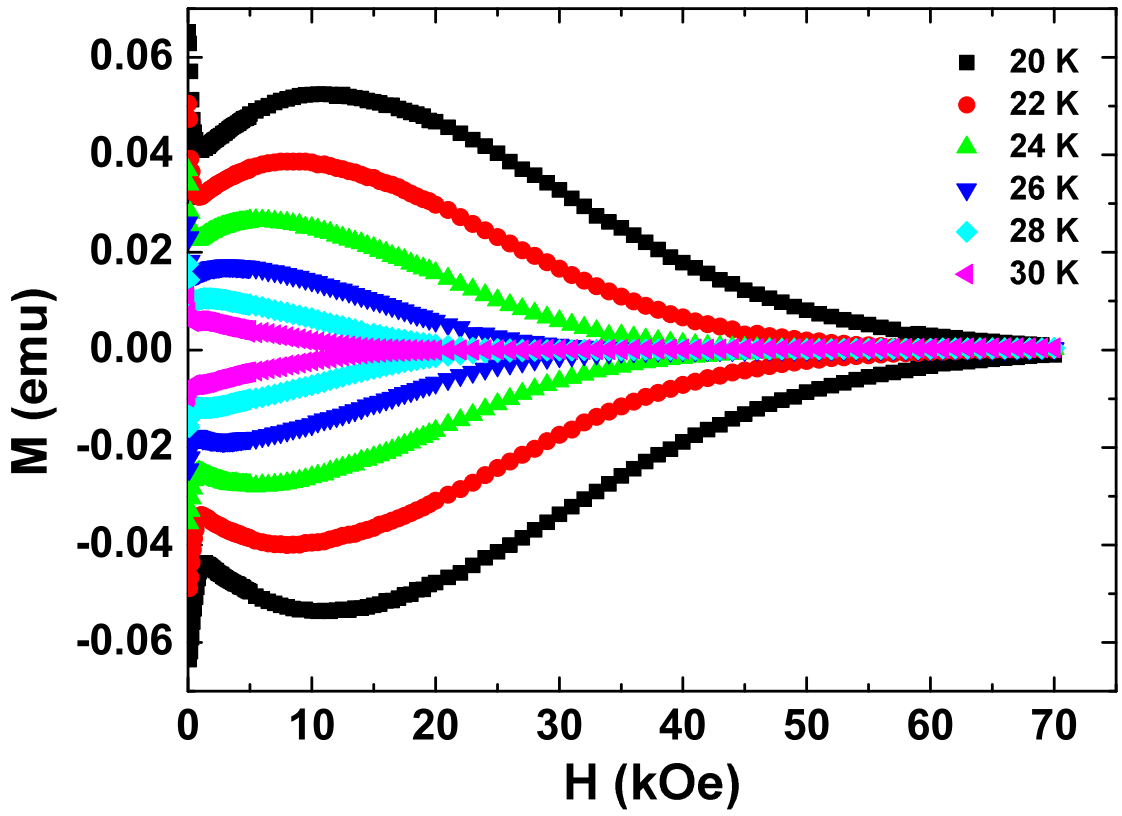

Figure 5.7: The field dependent magnetization taken at the temperature from 20 to 30 K with an interval of 2 K for $Ca_{10}Na_x(Pt_3As_8)(Fe_2As_2)_5$

[Fig5.8] shows the magnetic field dependent on critical current density (J_c) at the temperature from 2 K to 30 K with an interval 2 K. The J_c was calculated from magnetic hysteresis loops, using Bean's critical state model. The magnetic hysteresis loops are varying in the applied field from -7 to 7 T shown in [Fig5.6]. In the calculation results of the J_c, the $Ca_{10}Na_x(Pt_3As_8)(Fe_2As_2)_5$ has $4.7\times10^5 A/cm^2$ at 2 K. It is significantly two times larger than the J_c of the $Ca_{10}(Pt_3As_8)(Fe_2As_2)_5$, $2-3\times10^5 A/cm^2$[42]. And the critical current density is remarkably reduced as the proximity to the superconducting transition temperature. Therefore the $Ca_{10}Na_x(Pt_3As_8)(Fe_2As_2)_5$ single crystal could be applied more easily in the production of high magnetic fields than $Ca_{10}Na_x(Pt_3As_8)(Fe_2As_2)_5$.

As shown previously, the critical current density decreased according to the temperature. And the magnetic hysteresis loops indicated fish-tail effect between the temperature 20 and 30 K. These results suggest the importance on the study about the vortex behavior. The way to find out the pinning mechanism is obtained by using pinning force density as proposed by Dew-Hughes model. The pinning force density can offer much information about kind of pinning center. Dew-Hughes model describes a reasonable scaling law as $F_p \propto h^p(1-h)^q$ for conventional superconductors, where h is $h = H/H_{c2}$, H_{c2} is the upper critical field. But, in case of unconventional high transition temperature (T_c) superconductors are scaled as the irreversible field (H_{irr}) instead of the upper critical field, $h = H/H_{irr}$. Therefore, the pinning force density is associated with the irreversible field(H_{irr}), which is one of the key parameters that valuable information are given. We should be performed the scaling of the normalized pinning force makes it accessible to characterize the type of pinning center caused by defects in the sample. It is done based on the irreversible field, so it is a crucial factor in pinning mechanism.

There are several method of determination of irreversible field. First, we used Kramer

plot from $J_c^{0.5}H^{0.25} \propto (H_{irr} - H)$, are shown in [Fig5.9]. The irreversible field was determined from the extrapolation of linear fits, when $J_c^{0.5}H^{0.25}$ goes to zero[23][38]. Secondly, the irreversible field is estimated using the criterion of the critical current density[36][40]. Lastly, the case of unconventional high transition superconducting temperature is following the irreversible field of reference [43][44].

We can calculate the pinning force density following the this relation $F_p = J_c \times H$. [Fig5.10] shows that we plot the normalized pinning force, $F_p^{norm} = F_p/F_p^{max}$, as a function of the irreversible field using Kramer plot, $h = H/H_{irr}$. Also [Fig5.11] and [Fig5.12] shows the normalized pinning force employing criterion of the critical current density, $5\,A/cm^2$ and $10\,A/cm^2$, respectively. The last method of the irreversible field, which applying the reference, are shown in [Fig5.13]. Furthermore, the normalized pinning force is scaling well fitted.

We analyzed the flux pinning force with this fitted result by using Dew-Hughes model[26]. The Dew-Hughes model can classify the pinning mechanism according to the magnetic interaction and core interaction. There are the eight types of pinning mechanism that can be characterized by the different values of p and q.

[Fig5.10] shows that we plot the normalized pinning force, $F_p^{norm} = F_p/F_p^{max}$, as a function of the irreversible field using Kramer plot, $h = H/H_{irr}$ between 20 to 30 K. As shown in [Fig5.10], almost all indicates one fitting line within between the temperature 20 to 30 K.

The normalized pinning force curve can obtained by the scaling $F_p \propto h^p(1-h)^q$ with $p = 1.2$ and $q = 2.6$, $h_{max} = 0.33$, where h_{max} corresponds to the maximum pinning force (F_p^{max}). [Fig5.11] and [Fig5.12] show the normalized pinning force employing criterion of the critical current density, $5\,A/cm^2$ and $10\,A/cm^2$, respectively. It is the lowest value

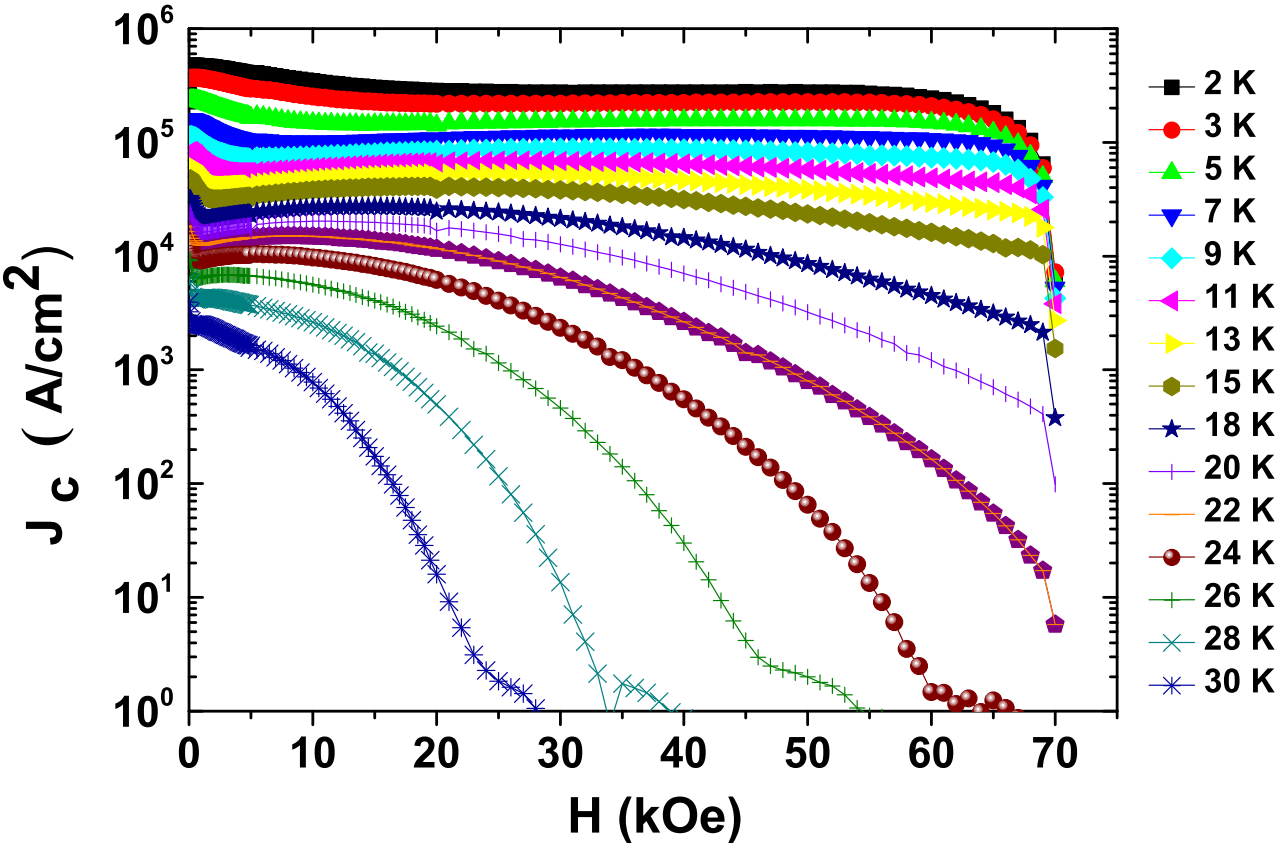

Figure 5.8: The Magnetic field dependence of critical current density J_c was estimated to the Bean model for $Ca_{10}Na_x(Pt_3As_8)(Fe_2As_2)_5$.

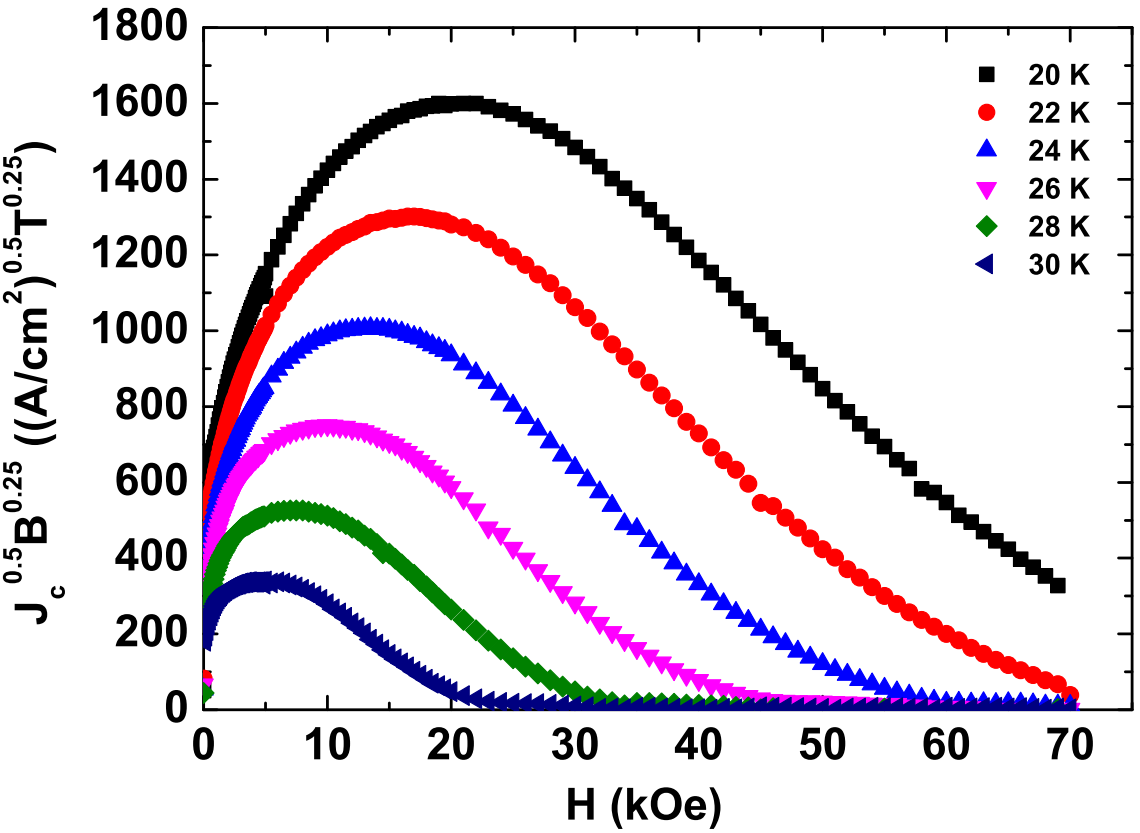

Figure 5.9: Kramer plot for $Ca_{10}Na_x(Pt_3As_8)(Fe_2As_2)_5$ in order to determine the irreversible field.

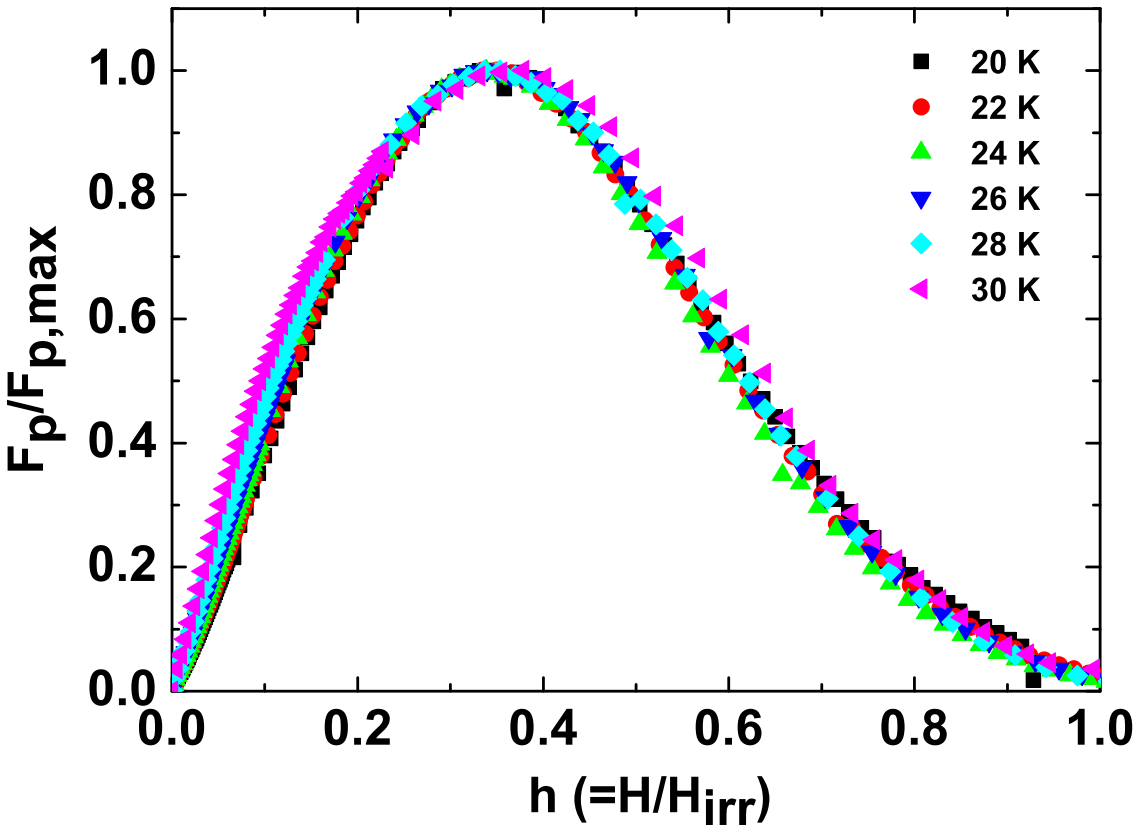

Figure 5.10: Scaling behavior of the normalized flux pinning force density, F_p/F_p^{max}, versus H/H_{irr} of $Ca_{10}Na_x(Pt_3As_8)(Fe_2As_2)_5$ using Kramer plot.

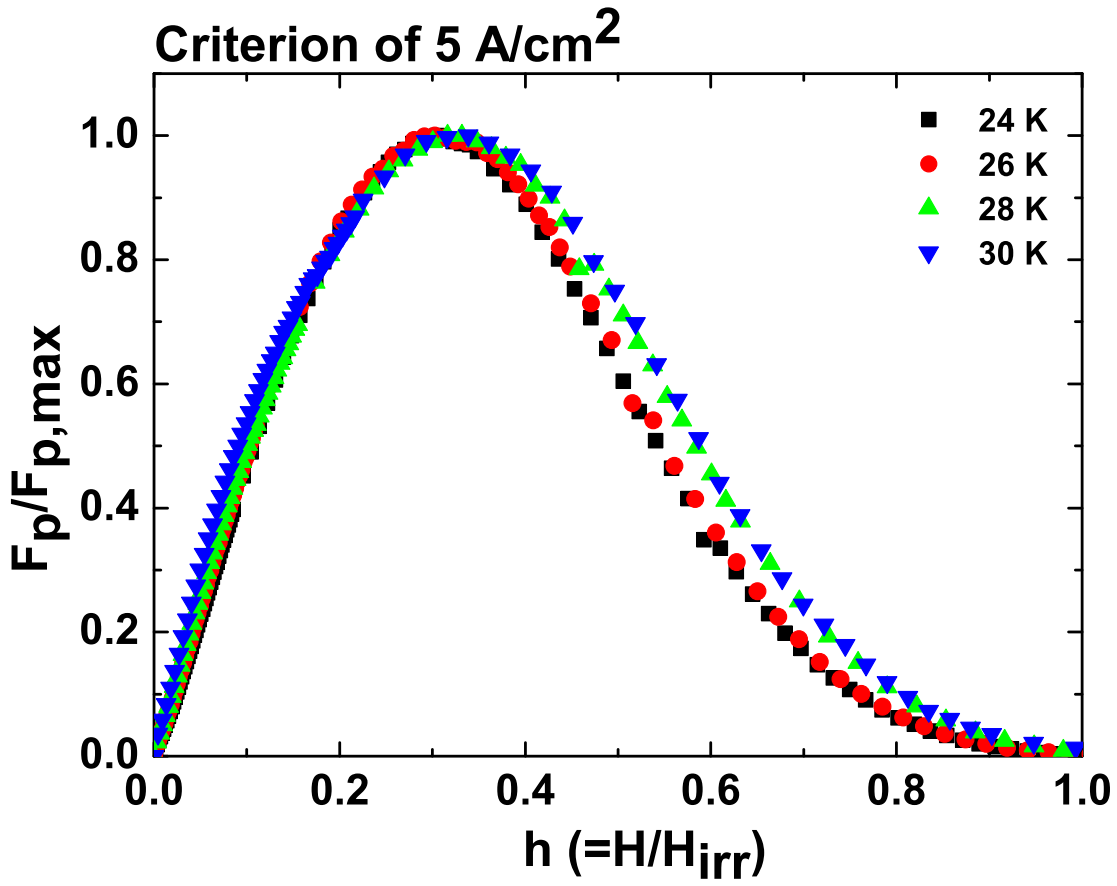

Figure 5.11: Scaling behavior of the normalized flux pinning force density, F_p/F_p^{max}, versus H/H_{irr} of $Ca_{10}Na_x(Pt_3As_8)(Fe_2As_2)_5$ using criterion of 5 A/cm^2

on the basis of the experimental data. It is observed that this normalized pinning force curves were overlapped into different temperature section.

In case of criterion of $5\,A/cm^2$, the temperature is divided into two parts in [Fig5.11]. The value of p and q is $p = 1.38$ and $q = 3.31$ at peak position of $h_{max} = 0.30$ in 24 and 26 K. The other parts in 28 and 30 K have $p = 1.21$ and $q = 2.63$, $h_{max} = 0.32$. The criterion of $10\,A/cm^2$ also is separated by the temperature 22, 24, 26 K and 28, 30 K in [Fig5.12]. The normalized pinning force curve fitting has value of $p = 1.36$ and $q = 3.02$ at peak position of $h_{max} = 0.31$ in 22, 24 and 26 K and $p = 1.10$ and $q = 2.26$, $h_{max} = 0.33$ in 28 and 30 K.

As shown in [Fig5.13], the irreversible field follows the reference. The normalized pinning force is well fitted by one curve regardless of temperature, between 20 and 30 K, and it has $p = 1.36$ and $q = 3.02$ at peak position of $h_{max} = 0.31$. Usually all fittings have the peak position almost $h_{max} = 0.33$ which means the point defects pinning center. $Ba_{0.6}K_{0.4}Fe_2As_2$ was observed the value of peak position $h_{max} = 0.33$[45]. This result suggests that it should have the normal cores because of arsenic deficiency. In addition, the high transition temperature superconductor, YBCO also has been explained as small size normal cores located at the peak position around the same value near fish-tail effect[43]. On the other hand, $BaFe_{1.8}Co_{0.2}As_2$ whose peak is $h_{max} = 0.45$ was reported to have relation with the inhomogeneous distribution of Co-ion[40]. Thus, we cannot simply use the peak position to exactly estimate the pinning mechanism. However, when viewed in a comprehensive manner, we should suggest that our sample has the normal core, where Na-ion acts as pinning defects in sample.

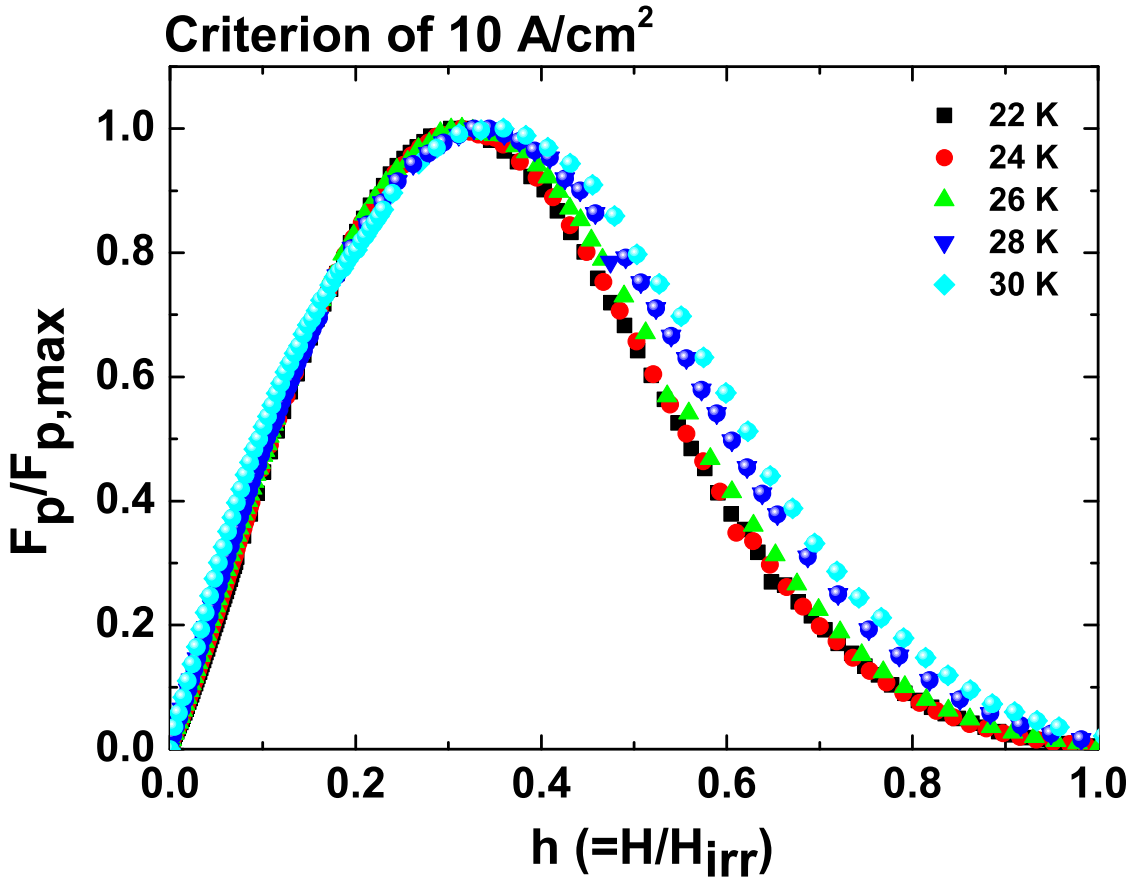

Figure 5.12: Scaling behavior of the normalized flux pinning force density, F_p/F_p^{max}, versus H/H_{irr} of $Ca_{10}Na_x(Pt_3As_8)(Fe_2As_2)_5$ using criterion of $10\,A/cm^2$

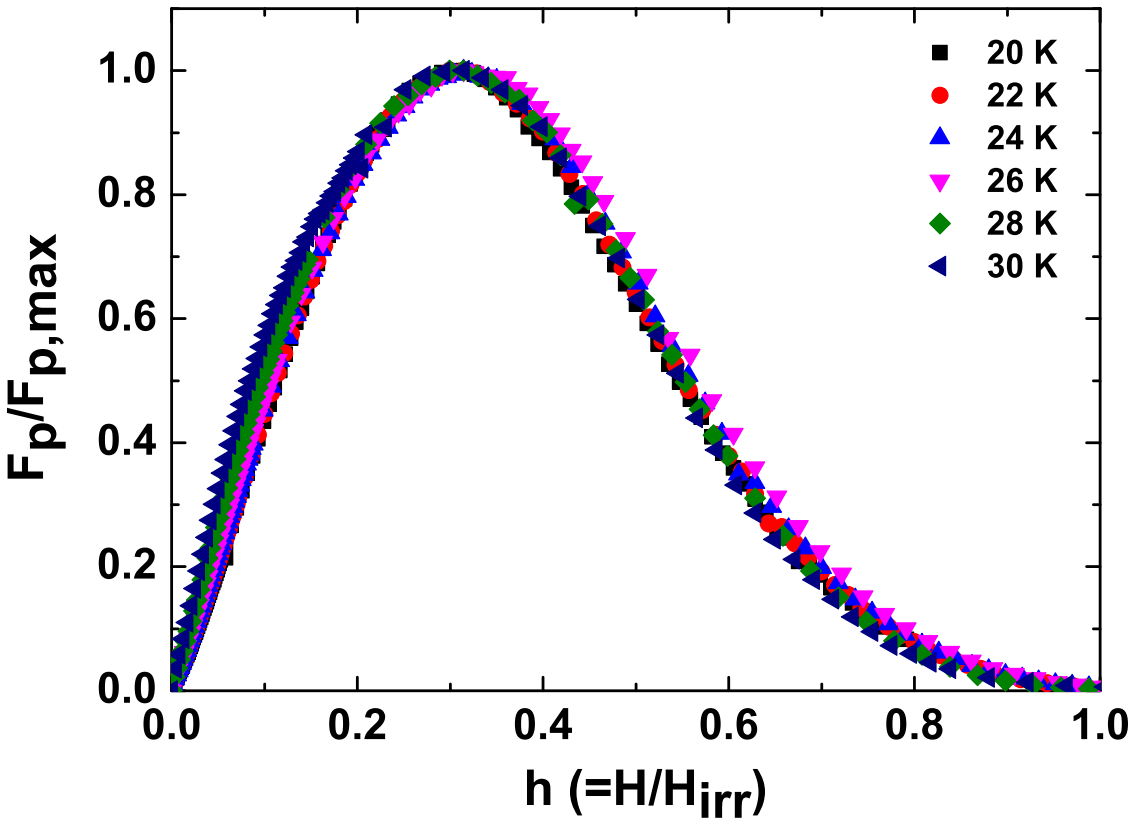

Figure 5.13: Scaling behavior of the normalized flux pinning force density, F_p/F_p^{max}, versus H/H_{irr} of $Ca_{10}Na_x(Pt_3As_8)(Fe_2As_2)_5$ by applying reference

Chapter 6. Conclusion

In this thesis, we report to study about flux pinning mechanism for $Ca_{10}Na_x(Pt_3As_8)$-$(Fe_2As_2)_5$ of single crystals. Unlike the iron-based superconductors reported, which were grown by the flux method, we successfully grew the single crystal with Bridgman method. Using the fabricated single crystal, we have confirmed the single crystal quality by X-ray diffraction (XRD) and a scanning electron microscopy (SEM) and we have measured transport property and a magnetic properties. The critical current density (J_c) was obtained using Bean's critical state model from Magnetization hysteresis loops, which has been carried out operating Quantum Design MPMS. The flux pinning force of $Ca_{10}Na_x(Pt_3As_8)(Fe_2As_2)_5$ single crystal had been investigated using Kramer model and Dew-Hughes model. Verifying the results, we can expect Na-ion intercalated on the $Ca_{10}Na_x(Pt_3As_8)(Fe_2As_2)_5$ single crystal that is longer in the c-axis direction by measuring XRD. It can be seen with SEM that it was well reacted by one phase to the surface and may be the content of Na-ion to be about 1.2. It shows the superconducting transition temperature (T_c) of 38.01 K in electrical resistivity and 37.07 K at low field of 20 Oe in magnetic susceptibility. Thereby, in comparison that $Ca_{10}(Pt_3As_8)(Fe_2As_2)_5$ was known as non-superconductor in existing reports, Na-ion intercalated in $Ca_{10}Na_x(Pt_3As_8)(Fe_2As_2)_5$ single crystal is distinct difference that superconductivity appears. And, also the transition temperature of $Ca_{10}Na_x(Pt_3As_8)(Fe_2As_2)_5$ has increased more than $Ca_{10}(Pt_3As_8)(Fe_2As_2)_5$ which is doped with Platinum. However, we expect that it does not look like perfect diamagnetism because Na-ion act as impurities.

The J_c was estimated by the magnetization hysteresis loops according to the Bean

model. The J_c for $Ca_{10}Na_x(Pt_3As_8)(Fe_2As_2)_5$ single crystal is 4.7×10^5 at 2 K, this value is about 2 or 3 times larger than $Ca_{10}(Pt_3As_8)(Fe_2As_2)_5$ single crystal. Therefore, this results will be anticipated be more achieved in application. Moreover, the fishtail effect was observed in $Ca_{10}Na_x(Pt_3As_8)(Fe_2As_2)_5$ single crystal between 20 and 30 K. The flux pinning force for $Ca_{10}Na_x(Pt_3As_8)(Fe_2As_2)_5$ single crystal obtains by various pinning model, such as Kramer model and Dew-Hughes model. The results of pinning force behaviors obeyed the scaling law and it could be well scaled in a functional form of $F_p \propto h^p(1-h)^q$. The scaling curves overlap well with the peak position located at around $h = 0.30 \sim 0.33$. The peak behavior of flux pinning force indicated that pinning center is normal core point defects from irreversible field, which is similar to the results in YBCO. Although it is hard to analyze the exact causes, Na-ion will be expected in role of impurities or structural defects similar to oxygen deficiency in YBCO. Finally, these results are really worthy in the iron-based superconductors. If this research progresses steadily in the future, it will provide much information of superconductivity mechanism.

References

[1] H. K. Onnes, "Further experiments with liquid helium. C. On the change of electric resistance of pure metals at very low temperatures, etc. IV. The resistance of pure mercury at helium temperatures", *Commun. Physc. Lab. Univ. Leiden*, 12, 120, 1911.

[2] W. Meissner and R. Ochsenfeld, "Ein neuer Effekt bei Eintritt der Supraleitfähigkeit", *Naturwissenschaften*, 3, 787, 1933.

[3] C. J. Gorter and H. G. B. Casimir, *Physics Z*, 35, 963, 1934; "In Progress in Low Temperature Physics", *Z. Tech. Phys.*, 15, 539, 1934.

[4] F. and H. London, "The electromagnetic equations of the superconductor", *Proceedings of the Royal Society of London*, A, 149, 71, 1935.

[5] 6. V. L. Ginzburg and L. D. Landau, "On the theory of superconductivity", *Zh. Eksp. Teor. Fiz.*, 20, 1064, 1950.

[6] J. Bardeen, L. N. Cooper, and J. R. Schrieffer, "Theory of Superconductivity", *Physical Review*, 108, 1175, 1957.

[7] J. G. Bednorz and K. A. Muller, "Possible high T_c superconductivity in the BaLaCuO system", *Z. Phys. B.*, 64, 189, 1986.

[8] C. W. CHU, L. GAO, F. CHEN, Z. J. HUANG, R. L. MENG, and Y. Y. XUE, "Superconductivity above 150 K in $HgBa_2Ca_2Cu_3O_{8+\delta}$ at high pressures", *Nature*, 365, 323, 1993.

[9] L. Gao, Y. Y. Xue, F. Chen, Q. Xiong, R. L. Meng, D. Ramirez, and C. W. Chu, "Superconductivity up to 164 K in $HgBa_2Ca_{m-1}Cu_mO_{2m+2+\delta}$ (m=1, 2, and 3) under quasihydrostatic pressures", Physical review B, 50, 4260, 1994.

[10] Y. Kamihara, T. Watanabe, M. Hirano, and H. Hosono, "Iron-Based Layered Superconductor $La(O_{1-x}F_x)FeAs$(x=0.05-0.12) with T_c 26 K", Journal of the American Chemical Society, 130, 3296, 2008.

[11] H. Hosono, "Layered Iron Pnictide Superconductors: discovery and current status", *Journal of Physical Society of Japan*, 77SC, 1, 2008.

H. Hosono, "Doping Dependence of Pseudogap in $LaFeAsO_{1`x}F_x$", *Journal of Physical Society of Japan*, 77, 063708, 2008.

[12] J. Paglione and R.L. Greene, "High-temperature superconductivity in iron-based materials", Nature Physics, 6, 645, 2010.

[13] C. Kittel, *Introduction to Solid State Physics, sixth edition*, Wiley, 2003, 258 pages.

[14] C. Kittel, *Introduction to Solid State Physics, sixth edition*, Wiley, 2003, 260 pages.

[15] C. Kittel, *Introduction to Solid State Physics, sixth edition*, Wiley, 2003, 264 pages.

[16] C. P. Bean, "Magnetization of hard superconductors", *Physical Review Letters*, 8, 250, 1962.

[17] C. P. Bean, "Magnetization of High-Field Superconductors", *Reviews of Modern Physics*, 36, 31, 1964.

[18] M. A. Tanatar, N. Ni, Martin, R. T. Gordon, H. Kim, V. G. Kogan,1 G. D. Samolyuk, S. L. Budko, P. C. Canfield, and R. Prozorov, "Anisotropy of the iron pnictide

superconductor $Ba(Fe_{1`x}Co_x)_2As_2$ (x=0.074, T_c=23 K)", *Physical Review B*, 79, 094507, 2009.

[19] Jung, S. G "Study of vortex dynamics in MgB_2", *Ph.D. Thesis*, Sungkyunkwan University, Suwon, Republic of Korea, 2010, 3 pages.

[20] http://scienceblogs.com/startswithabang/2011/10/22/weekend-diversion-lift-me-up-q/

[21] Y. B. Kim, C. F. Hempstkad, and A. R. Strnad, "Flux creep in hard superconductors", *Physical Review B*, 131, 2486, 1963.

[22] W. A. Fietz, and W. W. Webb, "Hysteresis in Superconducting Alloys-Temperature and-Field Dependence of Dislocation Pinning in Niobium Alloys", *Physical Review*, 178, 657, 1969.

[23] Edward J. Kramer, "Scaling laws for flux pinning in hard superconductors", *journal of Applied Physics*, 44, 1360, 1973.

[24] Teruo, and Matsushita, *Flux pinning in superconductors*, Springer Verlag, 2007, 313 pages.

[25] K. Yamafuji and F. Irie, "On the concept of pinning force in type-2 superconductors", *Physics Letters A*, 25, 387, 1967.

[26] D. Dew-Hughes, "Flux pinning mechanisms in type II superconductors", *Philosophical Magazine*, 30:2, 293, 1974.

[27] D. Dew-Hughes, "The role of grain boundaries in determining J_c in high-field high-current superconductors", *Philsophical Magazine Part B*, 55:4, 459, 1987.

[28] Teruo, and Matsushita, *Flux pinning in superconductors*, Springer Verlag, 2007, 287 pages.

[29] P. W. Bridgman, *Proceedings of the American Academy of Arts and Sciences*, 60 (6): 305, 1925.

[30] N. Hur, "Crystal Growth for the Research Purpose", Journal of Korean magnetics society, 21, 3, 2011.

[31] E. Kaldis, *Principle of the vapour growth of single crystal (Based on the manuscripy of a "Habilitationschrift")*, the ETH, 1972.

[32] http://en.wikipedia.org/wiki/Arsenic

[33] Dong-Jin Jang, A B Vorontsov, I Vekhter, K Gofryk, Z Yang, S Ju, J B Hong, J H Han, Y S Kwon, F Ronning, J D Thompson and T Park, "Calorimetric evidence for nodes in the overdoped $Ba(Fe_{0.9}Co_{0.1})_2As_2$", *New Journal of Physics*, 13, 023036, 2011.

[34] *Physical property measurement system resistivity option user's manual*, Quantum Design, 1999.

[35] N. Ni, Jared M. Allred, Benny C. Chan, and Robert Joseph Cava, "High T_c electron doped $Ca_{10}(Pt_3As_8)(Fe_2As_2)_5$ and $Ca_{10}(Pt_4As_8)(Fe_2As_2)_5$ superconductors with skutterudite intermediary layers", *PNAS*, 108, 45, E1019, 2011.

[36] H. Yang, H. Luo, Z. Wang, and H. Wen, "Fishtail effect and the vortex phase diagram of single crystal $Ba_{0.6}K_{0.4}Fe_2As_2$", *Applied Physics Letters*, 93, 142506, 015009, 2008.

[37] S. Sharma, K vinod, C S Sundar, and A Bharathi, "Critical current density and magnetic phase diagrams of $BaFe_{1.29}Ru_{0.71}As_2$ single crystals", *Superconductor Science and Technology*, 26, 2013.

[38] D. L. Sun, Y. Liu, and C. T. Lin, "Comparative study of upper critical field H_{c2} and second magnetization peak H_{sp} in hole and electron-doped $BaFe_2As_2$ superconductor", *Physical Review B*, 80, 144515, 2009.

[39] A. K. Pramanik, L. Harnagea, C. Nacke, A. U. B. Wolter, S. Wurmehl, V. Kataev, and B. Buchner, "Fishtail effect and vortex dynamics in LiFeAs single crystals", *Physcial Review B*, 83, 094502, 2011.

[40] A. Yamamoto, J. Jaroszynski, C. Tarantini, L. Balicas, J. Jiang, A. Gurevich, D. C. Larbalestier, R Jin, A. S. Sefat, M.A. McGuire, B. C. Sales, D. K. Christen, and D. Mandrus, "Comparative study of upper critical field H_{c2} and second magnetization peak H_{sp} in hole- and electron-doped $BaFe_2As_2$ superconductor", *Applied Physics Letters*, 94, 062511, 2009.

[41] M. Kano, Y. Kohama, D. Graf, F. Balakirev, Athena S. Sefat, Michael A. Mcguire, Brian C. Sales, D. Madrus, and Stanley W. Tozer, "Anisotropy of the Upper Critical Field in a Co-Doped $BaFe_2As_2$ Single Crystal", *Journal of the Physical Society of Japan*, 78, 084719, 2009.

[42] T. Tamegai, Q.P. Ding a, T. Taen, F. Ohtake, H. Inoue, Y. Tsuchiya, S. Mohan, Y. Sun, Y. Nakajima, S. Pyon, H. Kitamura, "Superconducting properties of iron–platinum–arsenides $Ca_{10}(Pt_nAs_8)(Fe_{2-x}Pt_xAs_2)_5$ (n = 3, 4) ", *Physica C*, 494, 65, 2013.

[43] L. Klein, E. R. Yacoby, and Y. Yeshurun, "Peak effect and scaling of irreversible properties in untwinned Y-Ba-Cu-O crystals", *Physical Review B*, 49, 4403, 1994.

[44] D. Ahmad,B. H. Min,S. Lee,G. C. Kim,Y. C. Kim,and Y. S. Kwon, "Critical current density and lower critical field in superconducting $Ca_{10}(Pt_4As_8)(Fe_{2-x}Pt_xAs_2)_5$ single crystal", *Superconductor Science and Technology*, 27, 075011, 2014.

[45] H. J. Kim, Y. Liu, Y. S. Oh, S. H. Khim, I. Kim, G. R. Stewart, and K. H. Kim, "Vortex-glass phase transition and superconductivity in an underdoped $(Ba,K)Fe_2As_2$ single crystal", *Physical Review B*, 79, 014514, 2009.

요 약 문

Vortex pinning force in superconducting Na-intercalated $Ca_{10}Na_x(Pt_3As_8)(Fe_2As_2)_5$ single crystal

1911년 Kamerlingh Onnes가 수은에서 초전도 현상이 발견 한 이후, 새로운 초전도체를 찾는 것을 110년 이상 수많은 연구들이 지속되고 있다. 특히 상업적으로 응용을 하기 위해서 고온 초전도체의 개발이 필수적이다. 지금까지 발견 된 초전도체 중에서는 구리 산화물계 초전도체가 상용 가능성이 높은 초전도 전이 온도(T_c)를 가지고 있으나, 산업에 이용되는 데에는 많은 어려움이 있다. 그러므로 다른 물질을 이용한 고온 초전도체의 발견이 매우 중요한 과제로 여겨져 왔다. 2008년 H. Hosono 그룹에 의해 LaOFeAs에 F를 도핑하여 26 K에서 초전도성이 보이는 철기반 초전도체가 발견된 이후, 철기반 초전도체의 전이온도는 56 K까지 상승하였다. 하지만 고온 철기반 초전도체를 개발이 필수적이지만 상용화를 위해서는 임계전류밀도(J_c)를 높이는 것 또한 중요한 요인이다. 임계전류밀도는 볼텍스(vortex)에 의한 영향을 받는다. 특히 볼텍스들의 움직임으로 인해 초전도체 내부에 열에너지가 발생하여 초전도 상태를 파괴할 뿐만 아니라 저항도 생성되어 임계전류밀도를 감소시킨다. 그러므로 초전도체 내에서 임계전류밀도를 최대화하기 위한 방법은 볼텍스 운동을 억제시켜야한다. 억제시키기 위한 방법 중 하나는 초전도체 내에 볼텍스 운동을 고정시키기 위한 피닝 센터(pinning center)를 만드는 것이다. 피닝센터의 역할을 알아보기 위해서는 초전도체 내에서 자속 꽂음힘(flux pinning force) 을 분석해야한다.

본 학위 논문에서는, 새로운 철기반 초전도체 중, 가장 최근에 발견된$Ca_{10}(Pt_3As_8)$-$(Fe_2As_2)_5$ 에 Na을 첨가하여 폐쇄형 브릿지만 방법으로 단결정을 성장시켰다. 새로운 철기반 초전도체에서 Na의 역할이 무엇인지 자속 꽂음힘(flux pinning force) 을 분석하였다.

폐쇄형 브릿지만 방법으로 $Ca_{10}Na_x(Pt_3As_8)(Fe_2As_2)_5$ 단결정을 성공적으로 성장시켰으며, 초전도 전이 온도가 37 K 에서 나타났다. 기존에 보고된 $Ca_{10}(Pt_3As_8)(Fe_2As_2)_5$ 보다 c- 축의 격자 상수가 길어진 것으로 보아 Na이 레이어 사이에 끼여있을 것이라 예상할 수 있다. 또한 EDS 측정 분석결과 Na이 약 1.2정도 함유되어있음을 예상 할 수 있다. 임계전류밀도는 자화 히스테리시스 측정 결과와 Bean's critical state model 을 통하여 계산하였다. 기존에 나타난 $Ca_{10}(Pt_3As_8)(Fe_2As_2)_5$ 보다 임계전류밀도가 약 2-3배 정도 상승하였음을 할 수 있다. Dew-Hughes model을 이용하여 자속 꽂음 힘 밀도(flux pinning force density) 그래프를 분석한 결과, $Ca_{10}Na_x(Pt_3As_8)(Fe_2As_2)_5$ 단결정의 경우에는 20 K 과 30 K 사이에서 점 결함들에 의한 자속 꽂음이 나타남을 알 수 있다. 이로서 기존의 $Ca_{10}(Pt_3As_8)(Fe_2As_2)_5$보다 Na을 첨가하였을 때, Na이 주요 꽂음 자리인 점 결함의 요인으로서 임계전류밀도를 향상 시킬 수 있다는 것을 보여준다. 이러한 결과를 바탕으로 볼텍스 움직임에 대한 연구가 지속되어 새로운 철기반 초전도체를 발견한다면, 초전도체를 이용한 산업에 이바지 할 수 있을 것이다.

핵심어 : 단결정 성장, 초전도체, 볼텍스, 임계전류밀도, 자속 꽂음